The Search for Extra Dimensions and the Atlas Forward Calorimeter

by
Guillaume A. N. Bélanger

A thesis submitted to the faculty of Graduate Studies and Research
in partial fulfilment for the degree of Master of Science

Ottawa-Carleton Institute for Physics,
Department of Physics, Carleton University
Ottawa, Ontario, Canada
October 4, 2002

The undersigned recommend to the Faculty of Graduate Studies and Research acceptance of the thesis

The Search for Extra Dimensions and the Atlas Forward Calorimeter

submitted by **Guillaume A. N. Bélanger, B.Sc.** in partial fulfilment of the requirements for the degree of Master of Science.

Chair, Department of Physics

Thesis Supervisor

Carleton University
October 4, 2002

Abstract

Models of extra dimensions such as the ADD model can be tested at the LHC with the ATLAS detector. Experimental consequences of such models include the production of Kaluza-Klein states of the graviton at TeV energy levels. Accurate detection of events with signatures of missing transverse energy as in graviton production, requires close to hermetic calorimetry coverage. The forward calorimeter in ATLAS is essential for this purpose. This thesis describes some features of models of extra dimensions and their signals in the context of the ATLAS calorimetry system with special emphasis on the forward calorimeter. The results of studies on the sensitivity of ATLAS to signals of extra dimensions showing that models like ADD will be confirmed or ruled out over a significant range of their parameter space at the LHC are discussed.

Acknowledgements

There are a number of people without whom I would not have been able to complete this thesis or my Masters degree. The person who has provided me with the most help and support is my spouse Kristin.

Professor Gerald Oakam has been a wonderful supervisor. His guidance and support complimented by his gentle ways have helped me tremendously, especially throughout the writing and editing of this thesis. I am very grateful to him for his help.

Professor Hans Mes, with whom I had the pleasure of working on the cabling of the FCal, has helped me with many technical issues related to the FCal and to calorimetry in general.

My close friend Dr. Ranpal Dosanjh has been a great resource for everything from relativistic kinematics problems to typesetting with LaTeX. His clarity of mind and his humour have often given me the strength to follow through on long and arduous tasks. I am very fortunate to have met Ranpal and very grateful to him.

David Waller, Mike Donkers and Dr. Mohsen Khakzad are three young physicists that have helped me with various problems on many occasions. Thomas Gregoire and Frédéric Leblond have helped me with theoretical issues related to the study of Extra Dimensions.

Finally the technical support provided by Bill Jack, Jim Carleton and Wade Hong to the physics department and that I have had the chance to enjoy for the last two years, has been a key element of my success in the masters program and I wish to thank them all very much for their professional and friendly assistance.

Contents

List of Tables

List of Figures

Chapter 1

Introduction

The intriguing possibility that the universe has a multi-dimensional spacetime structure that is more vast and more subtle than the conventional four-dimensional spacetime, has several experimental implications. These implications require a careful examination of the fundamental interactions between elementary particles at very high energy levels. An examination of this kind necessitates a new generation of particle accelerators such as the Large Hadron Collider, and powerful detectors like ATLAS, both under construction at this time.

Theories of Extra Dimensions (ED) include models where we live on a four-dimensional 'wall' or three-brane embedded in a vast multi-dimensional space or bulk through which only the as yet unobserved graviton can travel. They also include models in which this 'wall' is in fact more like a sheet folded over upon itself forming what appears to be parallel planes, or even theories in which there are many branes that float in the bulk and sometimes collide with one another causing enormous, Big Bang-like explosions. In some models of ED, the four fundamental forces of nature are said to unify into a single force at the TeV energy level. Gravity, by far the weakest of the four forces, becomes strong due to the ED, whose presence alters the gravitational potential at small distances or large energies. The testing of models such as these over a certain range of their parameters could be done at the Large Hadron Collider (LHC) with the ATLAS detector.

The primary aim of the ATLAS experiment is to use the full discovery potential of the LHC to uncover the mechanism responsible for giving particles their masses, and other new physical phenomena. The fundamental forces in the Standard Model (SM) of particle physics are part of a theory based on certain symmetries which must be broken in order to explain the different masses of the force carriers and also of the quarks and leptons. Why are photons and gluons massless, while W's and Z's are massive? The Higgs mechanism, named after the physicist who proposed it, offers an explanation for this and has its physical manifestation in the Higgs boson.

The gargantuan task of building a general purpose particle detector such as the ATLAS detector is made possible through a large international collaboration of physicists, engineers and technicians, and a high degree of coordination between the groups involved in the project. By the startup of the LHC and of ATLAS, planned for the year 2007, ATLAS will have been in the making for more than fifteen years and by the end of the experiment at least twenty five years will have passed. Scientific endeavours of this type help to illuminate the subtle and mysterious facets of the physical universe of which we are a part.

This thesis has two main foci. The first is an investigation into the search for signals of extra dimensions and the sensitivity of the ATLAS detector to such signals. The second is a synthesis of the work done on the cabling of the forward calorimeter, a sub-detector component of the ATLAS calorimetry system. The link between the search for ED and the forward calorimeter lies in the fact that some important signals of ED have characteristic signatures of missing energy in the final products coming from the primary proton-proton interaction. In order to maximise a detector's sensitivity to missing energy signals the largest possible coverage around the interaction point is sought. The forward calorimeter (FCal) covers the region just around the beam axis five meters from the interaction point (IP), where protons collide, thus contributing to an accurate energy reconstruction for events, and identification of jets of particles in the forward region.

The main purpose of this work is to show that the ATLAS detector is capable of imposing important experimental constraints on the range of values of parameters used in some models of TeV scale unification that include extra dimensions. Chapter 2 presents some basic aspects of physics in ED and an outline of one model of TeV gauge unification that includes ED. Events with signatures of missing transverse energy can only be detected through an accurate reconstruction of the energy of the decay products; calorimetry is essential for this task. The principles of calorimetry and of shower development in calorimeters are presented in Chapter 3. An overview of the ATLAS detector, its sub-detector components and their main characteristics is given in Chapter 4, and a more complete description of the forward calorimeter, including details of the construction and cabling, follows in Chapter 5. The methods used to detect and reconstruct missing transverse energy ($E_{\mathrm{T}}^{\mathrm{miss}}$), the component of the missing energy in the direction transverse to the beam axis, and the results of a number of studies on the sensitivity of the ATLAS detector to signals of ED are discussed in Chapter 6. Lastly, Chapter 7 offers a summary of the main points of this thesis.

Extra spatial dimensions and their implications on the fundamental interactions between constituents of matter are a potential source of exciting new physics. No evidence of the existence of more than three spatial dimensions has ever been reported by physicists, and the ATLAS detector at the LHC will offer one of the the first possibilities to search for such evidence. The startup of the Large Hadron Collider and of ATLAS in the year 2007 will mark the beginning of a new era in High Energy Physics that may shake the foundations of what we now believe, that will most likely provide answers to some unresolved questions in physics, and that will surely give rise to more questions about the nature of matter and of the elementary processes that make up this physical universe.

Chapter 2

Extra Dimensions

In physics, some theories and models are used to attempt to describe and explain what is observed.[1] These theories may then be subjected to experimental tests and evaluated according to certain standards of agreement with the experimental results. The construction of accelerators and colliders, together with particle detectors allows an investigation of the basic constituents of matter and the interactions between them. The LHC and the ATLAS detector will be extremely powerful tools in this investigation, and might even reveal evidence for tiny, hidden, extra spatial dimensions.

The hypothesis of the existence of more than three spatial dimensions is not new but has recently been revived as a means to address the so-called *Hierarchy Problem*. This chapter will introduce some key notions of physics in Extra Dimensions and present the essence of a model of ED proposed by Arkani-Hamed, Dimopoulos and Dvali in 1998.[2] The material presented in this chapter is not original. The manner in which it is presented is the result of the study of a number of papers on the topic, and an ongoing correspondence with other students. References on the topic of extra dimensions that were used and that do not appear

---

[1] Theory: A set of statements or principles devised to explain a group of facts or phenomena, especially one that has been repeatedly tested or is widely accepted and can be used to make predictions about natural phenomena.

Model: A schematic description of a system, theory, or phenomenon that accounts for its known or inferred properties and may be used for further study of its characteristics. [1]

as citations in the rest of this work include: [3], [4], [5], [6], [7], and [8].

2.1 Physics in Extra Dimensions

The world we inhabit appears to be four-dimensional. That is to say, if an arbitrary point is chosen as the origin, it is possible to uniquely specify the position of any point in spacetime with respect to the origin using four coordinates: three spatial and one temporal.[2]

In a Cartesian coordinate system, the three spatial variables x, y and z have dimensions of distance and range from $-\infty$ to $+\infty$. This corresponds to spatial dimensions with infinite size. Using a Cartesian model of the physical world, we must set a physical limit to the size of a space dimension; a limit to the spatial extent in a given direction. For this, we can assume that nothing contained in the universe can be larger in extent than the universe itself, and that spacetime expands with and as the universe, and thus setting the upper limit on the size of a spatial dimension to be that of the universe.

The actual size and shape of the three space dimensions in which we live is unknown to us. We know from observations that the universe is expanding but we do not know whether the rate of expansion is increasing, decreasing or constant. We believe that a 'slice' of the universe at a given moment in time appears as a three-dimensional hyper surface with no intrinsic curvature (flat), thus cartesian in topology. It is possible that the usual three dimensions are in fact curved, but current cosmology indicates that they are flat. In summary, we appear to live in a flat, expanding universe with three flat spatial dimensions of the size of the universe itself.

To introduce the notion of compact and periodic ED, consider a circle. For a given radius, the distance between two arbitrarily close points on the circumference of the circle can be written in polar coordinates as $ds^2 = R^2 d\theta^2$, where R is the radius and θ is the polar angle. (This line element is also often referred to as a metric). In this coordinate system,

---

[2] The three spatial dimensions that we usually think of as *the* three spatial dimensions, will be referred to as the 'usual' three spatial dimensions.

R ranges from 0 to ∞, and θ from 0 to 2π. Furthermore, R has dimensions of distance whereas θ is dimensionless. We can define a single variable $x = R\theta$, ranging from 0 to $2\pi R$ and having dimensions of distance, that gives rise to the same equation for the metric on the circumference of the circle. This illustrates that the circumference of a circle with fixed radius is one-dimensional and can be described by a single periodic variable x, with period $2\pi R$.

The preceding illustration can be used to hint at a conceptual notion of ED as follows. Imagine a one-dimensional space represented by a single straight, infinite line. If one extra compact and periodic dimension of radius R exists, then at every point on the line, space does not only extend over the infinite line in both directions but also over the circumference of a circle of radius R. If the circle is perpendicular to the line, then the overall topology is that of the surface of an infinite two-dimensional cylinder. In this cylindrical two-dimensional space, one dimension is flat and infinite, the other is compact and periodic with radius R.

As a three-dimensional example we can consider a flat, infinite two-dimensional space represented by an infinite, flat plane. Every point on this plane can be identified by two coordinates representing the distance between the point and the chosen origin in arbitrary units. An ED is introduced by specifying that a line transversely intersects every point on the plane. If the line is straight and infinite, the ED is said to be infinite and the overall space will be an infinite three-dimensional space or hypersurface akin to the one in which we live at a given moment in time. If the line forms a circle of radius R, then the ED is said to be compact and periodic with period $2\pi R$. The ED is said to be compact because it is curled up, and periodic because from a given point on the circle, $2\pi R$ is the proper distance that one travels in that direction before getting back to the starting point. It is possible to imagine any number of such circles or even any spheres and tori at every point on the plane. For each circular ED one additional coordinate is necessary to describe the location of a point in the space. For spherical ED, two additional coordinates are necessary. The size of a compact ED refers to the size of the radius whereas the size of a non-compact ED refers to its spatial extent.

In a number of models that include ED, the graviton, the force carrier for gravity, is taken to be the only particle that can propagate in all the spatial dimensions. Therefore, if our world is not a four-dimensional space but is in fact a six, seven or even eleven-dimensional space with tiny extra compact dimensions, then this could explain why gravity appears to be so weak on macroscopic scales. Since gravitons propagate equally in all dimensions, the probability of interaction in the usual three dimensions is low. A search for indirect effects of the gravitational interaction in ED on elastic electron-positron scattering at centre of mass energies between 183 and 209 GeV at LEP by the OPAL collaboration has led to a lower limit on the quantum gravity energy scale, of around 1 TeV. [9] Therefore, a higher energy collider like the LHC is necessary to test models of ED at the TeV scale.

Physics experiments show us that there appear to be four fundamental forces in nature: electromagnetic, weak, strong and gravitational. In particle physics, each one of these forces is mediated by what are called gauge bosons. The gauge boson or force carrier of the electromagnetic force is the photon γ. The carrier of the force of gravity is the graviton G. The weak and strong forces are mediated by more than a single gauge boson as in the case of the electromagnetic and gravitational forces. Indeed, there are three weak gauge bosons, the Z^0, W^+ and W^-, and eight mediators of the strong force called gluons g. Furthermore, the γ, G and g are massless while the weak gauge bosons are very massive. The strength of a force is described by a coupling constant, that may not be constant over the entire range.[3] At energy levels between 100 to 1000 GeV, the electromagnetic and weak forces can be described by a single theory. This energy level is called the *Electroweak* energy scale. They can thus be considered as a single *electroweak* force. In current theories, at energies around 10^{19} GeV, gravity is believed to become as strong as the other forces. This very high energy level is called the *Planck* energy scale, and also sometimes the quantum gravity energy scale.

---

[3] The values of the dimensionless coupling constants are given approximately as 0.53×10^{-38}, $\frac{1}{137}$, 1.02×10^{-5} and ~ 1, for the gravitational, electromagnetic, weak and strong forces respectively [10].

There is an enormous gap, of 16 orders of magnitude, between these two fundamental energy scales and how this arises is sometimes referred to as the *Hierarchy Problem.*

Extra dimensions address the Hierarchy Problem and the unification of gravity and the other forces by postulating that Standard Model particles are restricted to a three-brane embedded in a higher-dimensional space where only gravitons can propagate. Due to the large volume of the ED where gravitons can go, gravity appears to be very weak at low energies on the brane.

A common feature to all models with ED is the appearance of an infinite number of resonant states of certain particles. These are customarily referred to as Kaluza-Klein states (KK-states for short) or Kaluza-Klein modes, after the physicists who were the first to attempt to incorporate the electromagnetic force into a five-dimensional geometrized theory of gravity based on Einstein's General Theory of Relativity. *Every particle that can propagate in the extra dimensions will have an associated infinite tower of KK-states.* The appearance of these towers of resonances can be explained in the following manner: If we assume that momentum is quantised in all space dimensions, and that there is only one extra dimension that is compact, then a particle propagating in the extra dimension will carry only certain defined momenta, in direct analogy to quantisation in a resonant cavity. If a particle propagates in the ED with momentum p_5, the energy of this particle is given by:

$$E^2 = m_0^2 + p_4^2 + p_5^2 \tag{2.1}$$

where m_0 is the mass of the particle in its ground state in four dimensions.

Unfortunately, in a four dimensional world, we cannot measure p_5 and thus interpret this momentum as a mass as:

$$E^2 = m'^2 + p_4^2, \tag{2.2}$$

where $m'^2 = m_0^2 + p_5^2$. Since p_5 can take many different (quantised) values, in fact an infinite number of them, a particle that propagates in an extra dimension, looks like an infinite tower of massive particles.

The shape of the tower depends on the type of compactification. For example if the ED is compactified on a circle, the KK-modes are evenly spaced in mass with a spacing of $1/R$, where R is the radius of the ED. If the compactification is done on a sphere, then the shape is more complicated. A common feature to all models with ED is that the spacing between KK-modes scales inversely with the size of the ED. The larger the radius of the compact ED, the smaller the spacing between KK-states.

2.2 The ADD Model and some Experimental Implications

2.2.1 ADD

In 1998 Arkani-Hamed, Dimopoulos and Dvali (ADD) published a series of papers in which they presented a model of Large Extra Dimensions (LED). [2] [11] [12] The term large is used in the relative sense; large compared to the Planck scale.[4]

The main motivation of this model is to find a solution to the Hierarchy Problem. The authors posit that there is only one fundamental energy scale and that it is of the order of the electroweak scale $\sim 10^3$ GeV or 1 TeV. They explain that the reason why the force of gravity is so weak over distances greater than a centimetre is due to the existence of at least two compact and periodic ED of radius R much larger than the electroweak scale, 10^{-17} cm. Furthermore, the spacetime of the ADD model uses a flat metric and this makes it a reasonably simple model in terms of the mathematics involved. (See appendix B for a short introduction to the metric tensor). This section introduces the ADD model and discusses some of the its features and implications.

---

[4] The terms 'electroweak scale' and 'Planck scale' are used to denote energy scales as well as distance and time scales. In natural units $\hbar$ and c are set to unity and so we can move from units of energy to units of distance, to units of time simply by multiplying and dividing by these two constants. From the Planck energy $E_{\mathrm{PL}} = 1.22 \cdot 10^{19}\,\mathrm{GeV}$ we find the Planck distance by dividing by $\hbar = 0.197\,\mathrm{GeV} \cdot \mathrm{fm}$ and inverting to get units of distance. The Planck distance is given by $\mathrm{R}_{\mathrm{PL}} = 1.61 \cdot 10^{-33}\,\mathrm{cm}$. To get the Planck time, we simply divide R_{PL} by c and find $t_{\mathrm{PL}} = 5.38 \cdot 10^{-44}$. The electroweak distance is obtained in the same manner using $\mathrm{m}_{\mathrm{EW}} = 10^3\,\mathrm{GeV}$. We find $\mathrm{R}_{\mathrm{EW}} = 1.97 \cdot 10^{-17}\,\mathrm{cm}$.

In the ADD model, like in other models of ED, all SM particles are confined to a 4-D wall except the graviton which can propagate in the bulk. The presence of these ED alters the form of the gravitational potential as follows.
The Newtonian gravitational potential is given by:

$$V(r) \sim \frac{m_1 m_2}{\mathrm{M}_{\mathrm{PL}}^2} \times \frac{1}{r} \tag{2.3}$$

where m_1 and m_2 are two masses, r is the distance between them, and $\mathrm{M}_{\mathrm{PL}} = \sqrt{\hbar c / G_{\mathrm{N}}}$ is the four-dimensional Planck mass.

The gravitational potential in the presence of ED is given by the following equations:

$$V(r) \sim \frac{m_1 m_2}{\mathrm{M}_{\mathrm{PL(4+n)}}^{2+\mathrm{n}}} \times \frac{1}{r^{1+n}} \qquad r \ll R \tag{2.4}$$

$$V(r) \sim \frac{m_1 m_2}{\mathrm{M}_{\mathrm{PL(4+n)}}^{2+\mathrm{n}} R^n} \times \frac{1}{r} \qquad r \gg R \tag{2.5}$$

where R is the radius of the ED, n is the number of ED, and R^n is the volume of the extra dimensions.[5] $\mathrm{M}_{\mathrm{PL(4+n)}}$ is the multi-dimensional Planck mass, the quantum gravity scale, and the relationship between the four-dimensional and multi-dimensional Planck masses is found by comparing equations 2.3 and 2.5 for distances greater than 1 cm.[6] We thus find that the *effective* four-dimensional Planck mass is given by:

$$\mathrm{M}_{\mathrm{PL}}^2 = \mathrm{M}_{\mathrm{PL(4+n)}}^{2+\mathrm{n}} R^n \tag{2.6}$$

Equation 2.6 also gives the relationship between the fundamental energy scale and the size of the ED. If R^n is large, as it is assumed, then $\mathrm{M}_{\mathrm{PL(4+n)}}$ must be smaller than M_{PL}. Taking $\mathrm{M}_{\mathrm{PL(4+n)}} \sim 1\,\mathrm{TeV}$ and $n = 2$, we find that $R \sim 1\,\mathrm{mm}$.

2.2.2 Experimental Implications

If the quantum gravity energy scale is at the TeV scale, then this would certainly lead to interesting phenomena at this energy level. The Large Hadron Collider will run at centre of

---

[5] For simplicity, the radius of the extra dimensions is taken to be the same for all ED. The number of ED is not specified beyond the lower limit of at least two.

[6] The terms ‘Plank mass’, ‘Planck energy’, ‘Planck scale’ and ‘Planck energy scale’ have the same meaning and are used interchangeably.

mass energy of 14 TeV and will therefore probe the mass range from a few GeV to several TeV. Implications of the ADD model and of TeV scale quantum gravity include: direct graviton production, virtual graviton exchange, and mini black hole production. [13] [14] [15] [16] [17] (In this text the name 'Kaluza-Klein graviton' is usually suppressed in favour of simply 'graviton'). A number of Monte Carlo (MC) studies have been performed in order to estimate the sensitivity of the ATLAS detector to signatures of ED and the results of some of these studies will be presented in Chapter 6.

High energy proton-proton or pp collisions are complex but the majority of interactions are events with low momentum transfer referred to as minimum bias events. These can be viewed as the result of the colliding protons 'passing through' one another with minimal interaction. In the Standard Model, hadrons are made up of quarks floating in, and bound by, a strong field of eight gluons. Quarks and gluons are collectively called partons. Interesting events occur when two partons carrying a substantial portion of the proton's energy collide head-on resulting in significant momentum transfer. Furthermore, when there is enough energy in the interaction to break up the proton and free some of the quarks or gluons, those are detected as hadronic jets: conical sprays of hadrons. Figure 2.1 illustrates the four processes by which gravitons can be produced in pp collisions. Interactions involving graviton exchange are illustrated in Figure 2.2.

In the first diagram, Figure 2.1(a), a quark from one proton annihilates with a quark from the other proton and produces a graviton and a photon. This process leads to a signature of an isolated photon and missing transverse energy. Transverse energy is defined as the energy of a particle times the sine of the angle at which it hits the detector with respect to the beam axis. For small angles the approximation $sin\theta \simeq \theta$ is used and the missing transverse energy becomes $E_{\mathrm{T}}^{\mathrm{miss}} = E\theta$. In Figure 2.1(b), the two quarks annihilate and produce a graviton and a gluon. The gluon manifests itself as a hadronic jet and the graviton's presence is inferred by a transverse momentum imbalance. In 2.1(c), a quark from one proton interacts with a gluon from the other proton and produces a graviton and

(a) qq → Gγ

(b) qq → Gg

(c) qg → Gq

(d) gg → Gg

Figure 2.1: *Direct Graviton Production in pp collisions*

a quark. The quark, like the gluon, manifests itself as a jet, and the graviton is detected by the amount of energy it carries off into the bulk leaving a missing energy signal. And finally in 2.1(d), two gluons produce a graviton and a gluon. In three of the four processes of graviton production, the interaction between the two colliding partons takes place via the strong force through the exchange of a virtual gluon. Because gluons themselves carry colour, they couple directly to one another and there are three-gluon vertices and four-gluon vertices. [18] Therefore the interaction shown in 2.1(d) is allowed and its contribution to the cross-section must be considered. The time axis in all four Feynman diagrams is taken to be from left to right. In all cases of graviton production, the general topology of the $\mathrm{G} + jet$

(a) $\mathrm{qq} \rightarrow \mathrm{G}^* \rightarrow \mathrm{ff}$

(b) $\mathrm{gg} \rightarrow \mathrm{G}^* \rightarrow \mathrm{ff}$

(c) $\mathrm{qq} \rightarrow \mathrm{G}^* \rightarrow \mathrm{VV}$

(d) $\mathrm{gg} \rightarrow \mathrm{G}^* \rightarrow \mathrm{VV}$

Figure 2.2: *Virtual graviton exchange*

signal is quite simple for it gives rise to a single jet which is back to back in azimuth to balancing missing p_{T}. [19]

Figure 2.2 illustrates the four ways in which two colliding partons can interact and produce a pair of fermions or of vector bosons (γ's, W's or Z's), via a virtual graviton. The fermion or vector boson pair is produced as two quarks or two gluons annihilate. These processes are:

(a) $\mathrm{qq} \rightarrow \mathrm{G}^* \rightarrow \mathrm{ff}$: Two quarks annihilate and produce a virtual graviton that decays to a pair of fermions.

(b) $\mathrm{gg} \rightarrow \mathrm{G}^* \rightarrow \mathrm{ff}$: Two gluons produce a fermion pair via a virtual graviton.

(c) $\mathrm{qq} \rightarrow \mathrm{G}^* \rightarrow \mathrm{VV}$: Two quarks produce a pair of vector bosons.

(d) $\mathrm{gg} \rightarrow \mathrm{G}^* \rightarrow \mathrm{VV}$: Two gluons produce a pair of vector bosons.

The term 'virtual' in describing the graviton produced from the interactions in Figure 2.2, is used to describe a particle that has all the intrinsic properties of a graviton but that can have any mass. Such a virtual particle is said to be off its mass shell or simply, off shell. Once again, the time axis is taken to be from left to right. Graviton exchange would give rise to deviations from known cross sections for interactions producing two fermions or two vector bosons in the final state.

Kaluza-Klein states and the theoretical framework in which they arise in the presence of ED was briefly discussed in section 2.1. Most of the ATLAS studies involving KK-states have focused on KK gravitons, but a few studies have been done on KK gauge bosons, referred to here as γ^*, Z^* and W^*, not to be confused with the Z' and W' which usually symbolise heavy gauge bosons found in extensions to the SM.[7] (See references [15] and [20]). Both the Z^* and the W^* would decay through the same channels as their ground state partners, the Z and W, but would have large masses in the order of a few TeV. Possibly the most exciting proof of TeV scale quantum gravity and of the presence of LED would be the production of mini black holes at the LHC.

Mini black hole production can be summarised as follows: For a given mass $\mathrm{M_{BH}}$, it is possible to find an expression for the multi-dimensional Schwarzschild radius R_{S}, in the context of LED. Semi-classical arguments suggest that if two partons colliding with a centre of mass energy equal to $\mathrm{M_{BH}}$ and the impact parameter, (the distance between the two partons) is less than R_{S}, then a black hole of mass $\mathrm{M_{BH}}$ will form. [21] Black holes are said to decay "democratically" without preference, to all possible final state particles and would thus produce very unique signatures. Like for most yet unobserved physical phenomena, there are a number of different models of mini-black hole production. One such model presented by Dimopoulos and Landsberg in reference [21] predicts:

- Large cross-section

---

[7] Kaluza-Klein excitations are often denoted with an upper index in braces to indicate that there are many instances of the same particle with different masses. The graviton for example, is sometimes denoted $\mathrm{G}^{(n)}$ or $\mathrm{G}^{(k)}$.

- Hard, Prompt charged leptons and photons
- Little missing energy

Another model by Banks in reference [22] predicts at least three other very striking features of black hole production. These are:

- The average transverse momenta of jets should go down with the energy, precisely the opposite of the QCD expectation.
- Processes with transverse momenta larger than $1/R_{\mathrm{S}}$ should be completely absent.
- The Hawking decay of the final state would be nearly at rest in the centre of mass frame.

For more on black holes at colliders see references [23], [24], [25].

The ATLAS detector has been designed to have high sensitivity to missing transverse energy, the primary reason being that one of the two decay channels of the SM Higgs boson in the mass range $\mathrm{m_H} > 600\,\mathrm{GeV}$ expected to be observable above background is $\mathrm{H} \rightarrow \mathrm{ZZ} \rightarrow ll\nu\nu$. This decay channel requires excellent measurement of $E_{\mathrm{T}}^{\mathrm{miss}}$. [26] The nearly full calorimetry coverage of ATLAS and its extensive muon system make ATLAS a good detector for the study of any interaction giving rise to missing energy signals or electrons, photon and muons in the final state. The energy range that the LHC will cover, and that the ATLAS detector will probe , is from a few GeV to about 14 TeV. Much is not known about physics at the TeV scale and so this experiment will provide a window into a new world of high energy physics.

ADD and other models of gauge unification at the TeV energy level that include extra dimensions, will be tested in an independent manner with the LHC and ATLAS simply by taking a look at physics at these energies. More specific, model dependent studies will either confirm the hypothesis on which a certain model is based, or rule out a range of parameters for that model.

Chapter 3

Calorimetry

This chapter begins with a description of the basic principles of calorimetry, followed by a simple model of electromagnetic shower development in calorimeters. A discussion of the different types of calorimeters is presented in Section 3.2 and an overview of the basic features of liquid argon sampling calorimeters, as well as the calibration process for such a calorimeter is presented in 3.3.

3.1 Physical Principles

The Latin word *calor* means *heat*. A calorimeter then, is a device that measures 'heat' or energy. In particle physics, calorimeters are used to measure the energy of particles or groups of particles.

As most energetic particles travel through matter, they interact with the atoms in the medium and generate secondary particles, the secondary particles generate tertiary particles, and so on. Eventually all of the energy of the incident particle is dissipated through various processes in the medium. This cascade of particles from primary to secondary to tertiary and so on, is called a *shower*.

There are two types of showers: *electromagnetic* and *hadronic*. Incident photons, electrons and positrons give rise to electromagnetic showers; whereas hadrons like protons and charged pions give rise to hadronic showers. A general description of electromagnetic showers initiated by an electron (or a positron) can be expressed in the following way. The main processes that occur in an electromagnetic shower are *bremsstrahlung* and *pair production*. Bremsstrahlung or braking radiation is the name given to the radiation (or photons) emitted by electrons and positrons as they undergo acceleration. Pair production is the transformation of a photon into an electron positron pair. As a high energy electron travels through matter, it can interact electromagnetically with an atomic nucleus. This interaction can accelerate the electron causing it to radiate a photon which can carry a significant fraction of the electron's initial energy. As this photon travels through the medium it can, in the presence of a nucleus, convert itself to an electron positron pair. The electron and positron pair will each continue to travel through the medium, undergo electromagnetic interactions with the nuclei, and radiate photons. This repetitive process leads to the build up of the particles in the electromagnetic shower.

The moving charged electromagnetic particles in the shower continually lose energy by ionizing atomic electrons in the medium. As the shower develops, mostly longitudinally, the number of particles grows almost exponentially to a maximum depth t_{max}. At this point, most particles in the shower have an energy below a critical level and bremsstrahlung and pair production cease. This energy level is referred to as the *critical energy* (E_{c}) and is given approximately by:

$$E_{\mathrm{c}} = \frac{800\,\mathrm{MeV}}{Z + 1.2} \tag{3.1}$$

where Z is the number of protons in the atom. The maximum depth of the shower t_{max} is usually measured in units of the radiation length X_0. For electromagnetic showers, the customary parameterization is done in terms of radiation lengths as:

$$t_{max} = 3.9 + \ln E_0 \tag{3.2}$$

where t_{max} is measured in radiation lengths and E_0 in GeV. [27] X_0 is defined as the mean distance over which a beam of highly energetic electrons loses $(1 - 1/e)$ of its energy. Up to t_{max}, the transverse spread of the shower is less than one radiation length. Beyond that point the electrons are increasingly affected by multiple scattering, and the lateral size of the shower scales as the "Molière radius", given approximately by

$$\rho_{\mathrm{m}} \simeq \frac{7A}{Z}\,\mathrm{g/cm^2} \tag{3.3}$$

where A is the atomic mass. Roughly 95% of the shower is contained laterally in a cylinder of radius $2\rho_{\mathrm{m}}$. [27] When the energy of shower particles falls below E_{c}, they then lose the remainder of their energy through ionization and excitation in the medium.

Hadronic showers are initiated by energetic hadrons and the processes involved are different from those in electromagnetic showers. Charged pions can, for example, penetrate to quite a depth before interacting, thus delaying the shower development. Furthermore, hadronic secondaries; hadrons produced through the interaction of the incident hadron with a nucleus, can be highly energetic and in turn penetrate deeply without interacting. Most hadronic showers also have an electromagnetic as well as a hadronic component. For these reasons, there are large fluctuations in the depth of penetration in hadronic showers, and the phenomenology is much more complicated than for electromagnetic showers.

The longitudinal development of a hadronic shower is measured in absorption (or interaction) lengths given by $\lambda_{\mathrm{int}} = A/N_A\sigma_{\mathrm{abs}}$, where N_A is Avogadro's number, and σ_{abs} is the absorption cross-section. The interaction length is defined as the mean free path of a particle before undergoing an interaction that is neither elastic nor quasi-elastic (diffractive), in a given medium.

In hadronic showers, about half the energy of the incident hadron is transfered to additional fast secondary particles, and the rest goes to particle production, (mostly slow pions), and other processes. [27] Since secondary hadrons are produced with transverse momentum of about $\sim 350\mathrm{MeV}$, hadronic showers tend to be more spread out laterally than electromagnetic ones. Given the more penetrating nature of hadronic showers, hadronic calorimeters are typically located behind the electromagnetic calorimeters, furthest from the interaction point. A hadronic calorimeter must have sufficient material to minimize shower leakage from the back and often be corrected for the signal loss.

It is customary to parameterize the mean depth of a hadronic shower in units of nuclear interaction lengths in the medium as:

$$\lambda_{max} = 0.90 + 0.36 \ln E_0 \tag{3.4}$$

where λ_{max} is in interaction lengths and the energy E_0 is in GeV.

The use of this convention is a reflection of the fact that the two main processes responsible for the development of electromagnetic showers, bremsstrahlung and pair production, are both proportional to the radiation length X_0, whereas in hadronic showers the interactions that give rise to the shower are governed by the strong force and do not depend on the radiation length but rather on the nuclear interaction length λ_{int}.

3.2 Types of Calorimeters

In order to measure the energy of an incident particle, a calorimeter must stop the particle and generate a signal that can be converted into a measurement of its energy. These two functions are respectively called *passive particle absorption* and *active signal generation*. Directional information may be obtained by comparing the amplitude and timing of the signals collected from the different readout channels. The final stage is to establish a relationship between the measured signal and the energy of the incident particle. This is done through a calibration process.[1]

Electromagnetic calorimeters are built using high Z materials because $X_0 \propto 1/Z^2$. Hadronic calorimeters are built with dense materials because $\lambda_{\text{int}} \propto 1/\rho$. Absorber materials used in calorimeters such as copper, iron, lead and tungsten have nuclear interaction lengths of 15.06, 16.76, 17.09, 9.59 cm and radiation lengths of 1.43, 1.76, 0.56, 0.35 cm respectively. Whereas materials used as the signal-generating or active medium such as

---

[1] The calibration of calorimeters will be discussed in section 3.3.

polystyrene scintillating plastic and liquid argon have nuclear interaction lengths of 79.36 and 84.95 cm and radiation lengths of 42.4 and 14 cm respectively. Signal generation can be accomplished in different ways, some of which are discussed in the following paragraphs.

There are two types of calorimeters: *homogeneous* and *heterogeneous*. In homogeneous calorimeters, the functions of passive particle absorption and active signal generation are combined in a single material such as lead glass. Materials with this property are often used for electromagnetic calorimeters. In heterogeneous or *sampling* calorimeters, the functions of particle absorption and signal generation are separated. This type of calorimeter is made of alternating layers of passive and active materials. [28] The particles deposit the bulk of their energy in the passive layers and the signal is ‘sampled’ in the active layers (hence the name sampling calorimeter). A common type of sampling calorimeter is made with alternating plates of iron and scintillating plastic. The dense iron plates absorb energy and induce showers, and the scintillating plastic emits photons in proportion to the number of charged particles passing through it. These secondary photons, usually UV, are detected by photomultiplier tubes.

3.3 Liquid Argon Sampling Calorimeter

3.3.1 Basics

In a liquid argon (LAr) sampling calorimeter, evenly spaced layers of the passive medium or absorber, are immersed in LAr which acts as the active medium. As charged shower particles move through a parallel plate LAr sampling calorimeter, they pass through the absorber plates and through the LAr gap between the plates. In the LAr gap, the particles ionise atomic electrons, thus leaving electrons and positive ions in the active medium. A potential difference across the LAr gap forces the electrons to drift to the plates. The current generated by the moving charges temporarily changes the voltage across the gap causing a pulse in the voltage. This pulse is then transmitted to the electronics and constitutes a analog signal. Its amplitude is proportional to the initial current and the total charge collected on the anodes, which is in turn proportional to the amount of energy deposited by the incident ionising particle in the active medium.

The distance between the metal plates and the magnitude of the voltage across the gap determine the drift time: the time required for the electrons to migrate from their location in the LAr gap to the plates. The drift time determines the speed at which successive signals can be collected and thus affects the capacity to differentiate between sequential signals. The location of the calorimeter and the flux of interacting particles through it are important factors in the design of the detector. A discussion of the calibration of electromagnetic and hadronic calorimeters is presented in the paragraphs that follow.[2]

3.3.2 Calibration

Assuming complete containment of the shower, calibration is a procedure used to relate the output of a calorimeter to the energy of an incident particle of known type. The calibration can be divided in two parts, first the digital signal representing the output of the calorimeter must be related to a physical quantity such as the initial current $I_0 = I(t=0)$, or the total collected charge $Q = \int_0^{t_d} I(t)dt$, where t_d is the total drift time. This conversion does not depend on the incident particle type but on the characteristics of the electronics. Second, the physical signal I_0 or Q, must be related to the total energy deposited (E_{dep}) in the detector which can be related to the energy of the incident particle.

Electromagnetic Calorimeters

The following discussion illustrates how the charge collected in the calorimeter can be related to the total deposited energy. Consider a parallel plate LAr/Cu electromagnetic calorimeter with plates of constant thickness d_{abs}, and constant plate separation d_{gap}. The unit of sampling distance is then given by $d = d_{\text{abs}} + d_{\text{gap}}$. Signals are generated in, and collected

---

[2] The discussion of the calibration of electromagnetic and hadronic calorimeters is based on reference [29].

from the active medium only, and so the total signal produced in the gap is proportional to the number of crossings of charged particles through this gap. For a given signal, the total number of tracks left by charged particles is related to the total track length of all the tracks in the electromagnetic shower. The total number of charged crossings N_{cross}, total charged track length T_{c}, and total track length T, are related in the following manner:[3]

$$T_{\text{c}} = \frac{2}{3}T \quad \text{and} \quad N_{\text{cross}} = \frac{T_{\text{c}}}{d} \tag{3.5}$$

The energy lost by a single charged particle crossing the active medium, is equal to the energy loss per unit path length in the active medium times the length of the gap. It is given by:

$$\Delta E = \tfrac{dE}{dx}|_{\text{act}} \cdot d_{\text{act}} = \text{const} \tag{3.6}$$

and is assumed to be constant for simplicity. Therefore, the total energy deposited in the active medium, the visible energy E_{vis}, and the total energy deposited in the calorimeter are related as follows:

$$E_{\text{vis}} = N_{\text{cross}} \cdot \Delta E = S \cdot E_{\text{dep}} \tag{3.7}$$

where S is called the *sampling fraction* and is defined as the ratio $E_{\text{vis}}/E_{\text{dep}}$. Finally, a calibration function is used to relate the measured deposited energy to the actual energy of the particle.

The assumptions about the development of electromagnetic showers in a calorimeter used to derive equations 3.6 and 3.7 form the basis of what is known as Rossi's model. These assumptions are:

1. Energy loss per unit path length is constant for electrons, and so both $\frac{dE}{dx}|_{\text{act}}$ and $\frac{dE}{dx}|_{\text{abs}}$ are constants;
2. The shower is taken to develop in one dimension only;

---

[3] The factor of $\frac{2}{3}$ arises from the assumption that electromagnetic showers are composed of electrons, positrons and photons in equal number, and on the fact that only the electrons and positrons leave charged tracks. Therefore, the number of charged tracks, T_{c}, is $\frac{2}{3}$ of the total track length, T.

3. Compton scattering, i.e. scattering of photons on electrons, is ignored.

Although most simple models of electromagnetic showers are based on similar simplifications, such models can be useful for describing the general behaviour of showers and doing approximate calculations. Nevertheless, most theoretical models used for calibration are inadequate and in practice, the calibration process is usually done with a test beam and completed with real data. By directing particles of known energies and momenta at various angles on different parts of the calorimeter, the shower shape can be reconstructed using the signals collected from the different segments of the detector. Depending on the performance requirements of the calorimeter, shower containment can be estimated and a calibration function relating E_{dep} to the actual particle energy can be derived.

Hadronic Calorimeters

The procedure used in calibrating hadronic calorimeters is similar to that of electromagnetic ones. An illustration of some issues related to the calibration of hadronic calorimeters is presented in the following section. The illustration uses an example of a hadronic shower initiated by a π^+, and will mostly serve to highlight the variation of the sampling fraction in hadronic showers. The large fluctuations in sampling fraction from one hadronic shower to another, make up the largest contribution to the resolution of a hadronic calorimeter, and make it very difficult to model the shower precisely, thus making the calibration more complicated.

Although hadronic showers differ significantly from electromagnetic ones, hadronic signals, like electromagnetic ones, are generated by charged particles crossing the active medium, and can thus be understood as the sum of all the energy ΔE deposited in the active medium. The important difference between electromagnetic and hadronic shower signals is that, in hadronic showers, not all deposited energy can be converted into a signal. The assumption that $N_{\text{cross}} \propto \frac{2}{3}T$, is no longer appropriate since the fraction of the total track length T, which contributes to the signal varies substantially from one shower to another. This can be explained by considering two possible outcomes of a hadronic shower initiated by a charged pion.

An energetic π^+ penetrates the calorimeter, possibly quite deeply, and interacts with a nucleus. The interaction can give rise to π^0 + p or π^+ + n. The π^0 will decay to a pair of photons almost immediately thus giving rise to two electromagnetic showers, whereas the π^+ is very unlikely to decay and will give rise to other hadronic processes as it deposits its energy in the calorimeter. Some of these hadronic processes can be penetrating while others less so. And so the two showers will be significantly different.

This example helps to illustrate the large fluctuations in the sampling fraction that can occur from one hadronic shower to another, and how this in turn invalidates the assumption that $N_{\text{cross}} \propto \frac{2}{3}T$. Furthermore, there is typically more leakage in hadronic showers than in electromagnetic ones, making the calibration even more difficult. Thus, precise calibration of a hadronic calorimeter can be a complicated and lengthy procedure.

Calorimeter Resolution Contributions

The final signal from a detector is the number of electrons that are registered in the electronic circuits. The resolution of the device for detecting an incident particle of energy E_0 is determined by fluctuations in the number N of these electrons. These fluctuations can arise from: [27]

1. sampling fluctuations, (fluctuations in the amount of energy deposited in the active medium);
2. leakage of energy out of the calorimeter;
3. noise in the active medium;
4. electronic noise;
5. pile-up.

If these fluctuations follow a Poisson distribution, the standard deviation is $\sigma(N)/N = 1/\sqrt{N}$. The main contribution to the energy resolution of electromagnetic calorimeters is usually sampling fluctuations. In general, the resolution of hadronic calorimeters is worse than that of electromagnetic calorimeters. Hadronic calorimeters are subject to all the fluctuations found in electromagnetic showers, and fluctuations due to nuclear interactions. Also, the energy used for the production of neutrinos and high energy muons, represent energy that 'escapes' from the calorimeter. Variations in the importance of these processes represent a major contribution to the resolution of hadronic calorimeters.[27]

In a hadronic detector like the FCal, pile-up is a major concern. Since pile-up is constituted by overlapping signals from more than one event within the time resolution of the detector, the most direct way to reduce pile-up is to reduce the signal integration time; the faster the signals are collected, the less overlap there is. In addition, there is electronic noise which is related to the capacitance of the electrode elements. The higher the capacitance, the higher the electronic noise. Furthermore, electronic noise increases with decreasing shaping time and so the optimum shaping time is found by comparing the decrease of electronic noise and increase in pile-up with increasing shaping time. A typical optimisation plot is shown in Figure 3.1

The energy resolution of a detector can be parametrised as

$$\frac{\Delta E}{E} = \frac{a}{\sqrt{E}} \oplus \frac{b}{E} \oplus c \tag{3.8}$$

where E is in GeV, a is the sampling or stochastic term, b is the noise term, and c is the constant term. The sampling term refers to the fluctuations of the actual energy deposited in the active layers of the detector for a given particle type at a given energy. The noise term refers to contributions from electronics noise and pile-up related to the capacitance of the electrodes and the active gap width, and the signal integration time. Finally the constant term, includes all factors that are due to inherent features of the detector.

Figure 3.1: *Optimisation of signal pulse shaping time at the LHC for high and low luminosity.*

Chapter 4

The ATLAS Experiment

This chapter provides an overview of the LHC machine and ATLAS detector. A brief summary of the features and design parameters of the LHC machine are presented in Section 4.1, and a more detailed description of the ATLAS detector and of its sub-detector components is given in 4.2. The sources used in writing this chapter are the ATLAS Letter of Intent, Technical Proposal, and Technical Design Reports; references [30], [31], [32], [33], [34], [35], [36], [37], and [26].

4.1 The Large Hadron Collider

The Large Hadron Collider is a high energy, high luminosity proton-proton machine. It is the highest energy collider ever to be built with a centre of mass energy of 14 TeV and has a design luminosity of $2.3 \cdot 10^{34}$ interactions/ $\mathrm{cm}^2 \cdot \mathrm{s}$. The experiment is scheduled to run for the first three years at a luminosity of $\sim 10^{33}\,\mathrm{cm}^{-2} \cdot \mathrm{s}^{-1}$ and for at least ten years at the design luminosity. The infrastructure is provided by CERN, the European Organisation for Nuclear Research, and the LHC is being built in a tunnel with a circumference of 27 km that was used for a previous accelerator, the Large Electron-Positron or LEP collider.

The LHC machine will accelerate 2808 bunches of 10^{11} protons with spacing a of 7.48 m

Figure 4.1: *Three-dimensional view of the ATLAS detector. Some muon chambers and parts of the barrel toroid are removed to show the inner structure.*

in each ring of the collider. These bunches will cross every 25 ns giving rise to about 18 interactions/ns at the design luminosity The beam has a transverse size of $15.9\,\mu$m and cross-sectional area of $6.5 \cdot 10^{-25}\,\mathrm{cm}^2$. This very high collision rate is the source of important data acquisition challenges.

4.2 The ATLAS Detector

The ATLAS experiment is the largest collaborative effort ever attempted in the physical sciences. The collaboration, composed of about 2000 scientists from more than 150 universities and research laboratories in 34 countries worldwide, is building the biggest and most complex detector ever built. ATLAS is one of two large detectors at the LHC and its completion is scheduled to occur in the course of the year 2007.

The basic design considerations for ATLAS are summarised in the Technical Proposal as follows: [31]

- high resolution electromagnetic calorimetry, complemented by hermetic jet and missing E_{T} calorimetry;
- Efficient tracking at high luminosity;
- precision muon-momentum measurements;
- large acceptance in η coverage;[1]
- triggering and measurements of particles at low-p_{T} thresholds.

4.2.1 Physical Parameters

The overall dimensions of the enormous, cylindrically shaped, ATLAS detector are 42 m in length and 22 m in diameter with an overall weight of about 7 000 tons.

The outermost components of the ATLAS detector make up the muon system, and thus its position and size define the overall size of the detector. The innermost components are the precision tracking elements consisting of a barrel part and two identical forward parts. The inner detector occupies the cylindrical cavity defined by the boundaries of the cryostats housing the electromagnetic calorimeters. The dimensions of this cavity and thus of the inner detector are 7.0 m in length and 2.3 m in diameter. All other detectors between the inner cavity and the muon chambers are electromagnetic and hadronic calorimeters. The calorimetry system has a weight of about 4 000 tons or 57% of the total weight of the ATLAS detector. The overall performance goals for the ATLAS detector are summarised in Table 4.1.

4.2.2 Magnet Systems

The ATLAS superconducting magnet systems consist of one central solenoid magnet enclosing the inner cavity and providing the magnetic field for the inner detector, and three large air-core toroids that generate the magnetic field for the muon spectrometer.

---

[1] Further details on the pseudo-rapidity variable η are given in appendix A.

Table 4.1: *General ATLAS detector performance goals. The minimum required resolution and the coverage in η for each of the four main sub-detector systems are shown. The resolution is stated as the sampling term plus the constant term.*

Detector component	Minimum resolution requirements	η coverage	
		Measurement	Trigger
EM calorimetry	Energy: $\frac{\Delta E}{E} = \frac{10\%}{\sqrt{E}} \oplus 0.7\%$	$\lvert\eta\rvert < 3.2$	$\lvert\eta\rvert < 2.5$
Jet and missing E_{T} Calorimetry			
barrel and end-cap	Energy: $\frac{\Delta E}{E} = \frac{50\%}{\sqrt{E}} \oplus 3\%$	$\lvert\eta\rvert < 3.2$	$\lvert\eta\rvert < 3.2$
forward	Energy: $\frac{\Delta E_{\mathrm{T}}}{E_{\mathrm{T}}} = \frac{100\%}{\sqrt{E}} \oplus 10\%$	$3.1 < \lvert\eta\rvert < 4.9$	$3.1 < \lvert\eta\rvert < 4.9$
inner detector	Momentum: $\frac{\Delta p_{\mathrm{T}}}{p_{\mathrm{T}}} = 30\%$ at $p_{\mathrm{T}} = 500\,\mathrm{GeV}$	$\lvert\eta\rvert < 2.5$	
Muon detection	Momentum: $\frac{\Delta p_{\mathrm{T}}}{p_{\mathrm{T}}} = 10\%$ at $p_{\mathrm{T}} = 1\,\mathrm{TeV}$ in stand-alone mode at highest luminosity	$\lvert\eta\rvert < 2.7$	$\lvert\eta\rvert < 2.4$

The solenoid magnet is integrated in the vacuum vessel of the liquid argon calorimeter barrel cryostat. Wound as a single layer with radius 1.22 m and length 5.3 m, the solenoid has an axial field strength of 2 T. The coil together with the cryostat wall placed in front of the electromagnetic calorimeter have a total thickness in radiation lengths of $0.83\,X_0$ at normal incidence.

The superconducting air-core toroid magnet system consists of three parts, a barrel and two end-caps, housed in ten cryostats. The barrel part is 26 m long, has an outer diameter of 19.5 m and inner bore of 9.4 m. It is made of eight flat coils symmetrically arranged about the beam axis, each contained within a separate cryostat. The end-caps, each housed in a separate cryostat, are inserted into each end of the barrel, and have a length of 5.6 m with inner bores of 1.26 m.

The air-core magnet system forms one solid structure and represents a cold mass of about 700 tons. It provides an azimuthal field with a total bending power integrated between the first and last muon chambers increasing from 2 Tm at $\eta = 0$ to about 8 Tm at $|\eta| = 2.7$.

Figure 4.2: *Superconducting air-core toroid magnet system. The left-hand end-cap toroid is shown retracted from its normal operating position. Only one of the cross-braces of the barrel toroid is shown in full detail. A person is shown standing between the end-cap toroid and the barrel structure to provide a size scale for the magnet system.*

Figures 4.2 and 4.3 show schematics of the superconducting air-core toroid magnet system.

4.2.3 Sub-detector Components

Inner Detector

The task of the inner detector is to reconstruct the tracks and vertices in the event with high efficiency, contributing, together with the calorimeter and muon system to the electron, photon and muon recognition, and supplying the important extra signature for short-lived particle decay vertices. [35] This is achieved by integrating two detector technologies in the design of the inner detector: Semi-Conductor Tracking (STC), and Transition Radiation Tracking (TRT).

Figure 4.3: *End view of the magnet system. A cut view of the end-cap toroid cryostat is shown inserted in between the barrel toroid coils.*

The STC comprises silicon pixel detectors closest to the interaction region, and silicon-strip detectors for precision tracking. The detector is divided into a barrel part and two identical end-caps. In the barrel there are two pixel layers and four silicon strip layers before the straw tubes. In the end-caps, there are four pixel disks and nine silicon strip wheels. The TRT or straw tube tracker provides continuous track measurement further from the interaction point, as well as enhanced electron identification by employing xenon gas to detect transition radiation photons. Each track crosses at least three pixel, and four strip layers before passing through the TRT which typically gives 36 points per track. [35]

The overall transverse momentum resolution of the inner detector as a function of η for charged tracks with $p_{\mathrm{T}} = 500\,\mathrm{GeV}$ is shown in Figure 4.4. [35] The solid curve shows the momentum resolution for a uniform magnetic field of $2\,\mathrm{T}$ and the dashed curve for the real solenoidal field. As can be seen from the plot, the overall resolution is around 35% up to about $|\eta| = 2$ and increases rapidly for $|\eta| > 2$. The deterioration is due to the weakening of the magnetic field near the ends of the solenoid.

Figure 4.4: *The inner detector momentum resolution vs.* η *for tracks with* p_{T} *=500* GeV*, for the real solenoidal field compared to a uniform 2* T *field.*

Muon Spectrometer

The precision muon system, has tracking detectors with intrinsic resolution of about 60 μm. Emphasis is given to reliable, high resolution, stand-alone performance over a p_{T} range from about 5 to 1000 GeV. [31] The superconducting air-core magnet system described in Section 4.2.2 is the basis of the muon spectrometer. There are fast chambers for triggering, and slower chambers for precision momentum measurements. The large area covered by muon chambers must be shielded by the inner parts of the detector and the FCal is essential for shielding from the very high particle density in the forward regions.

The main parameters of the muon spectrometer are summarized in Table 4.2, and a plot of its transverse momentum resolution as a function of η is shown in Figure 4.5. The p_{T} resolution is plotted for tracks with p_{T} =100 GeV averaged over all azimuthal angles. The solid curve applies to a standard octant, the dotted curve corresponds to one of the bottom octants that contain the feet. Loss in resolution may be due to fewer chambers and to distortion of the magnetic field from the steel support feet.

Table 4.2: *Principal parameters of the muon spectrometer*

Parameter	Main physics criteria	Performance		Comments
		desired	actual	
Momentum measurement				
Δp_{T} @ 20 GeV	$\mathrm{H} \rightarrow \mathrm{ZZ}^{*} \rightarrow 4l$	$< 1\%$	2%	Limited by energy loss and multiple scattering
Δp_{T} @ 100 GeV	$\mathrm{H} \rightarrow \mathrm{ZZ} \rightarrow 4l$	$< 1\%$	2%	Multiple scattering limit
Δp_{T} @1000 GeV	$\mathrm{Z}' \rightarrow \mu\mu$	$< 1\%$	8%	Global detector optimisation
Rapidity coverage	Above processes	$\lvert\eta\rvert \leq 3$	$\lvert\eta\rvert \leq 3$	Entire System

Figure 4.5: *Transverse momentum resolution of the muon spectrometer as a function of pseudo-rapidity* η. *The discontinuities are caused by the structural elements of the barrel toroid magnet.*

Figure 4.6: *Three-dimensional view of the ATLAS calorimetry system from the* `GEANT` *simulation program.*

Calorimetry System

The ATLAS calorimetry system is a high performance system capable of reconstructing the energy of electrons, photons and hadronic jets, as well as measuring missing transverse energy. Its radiation resistance allows for more than ten years of data taking at the LHC during the high luminosity phase. [31]

The stringent performance requirements placed on the calorimetry system are based on the most demanding decay channels of the Higgs boson, namely H $\rightarrow \gamma\gamma$ and H $\rightarrow$ ZZ $\rightarrow 4e$, and on the detection of new very massive gauge bosons. Below is a brief description of the detector components of the calorimetry system, their location in the ATLAS detector, their η coverage, and their respective resolutions.

The calorimeters are grouped within four sections of ATLAS: the barrel or central region, the extended barrel, and the two end-caps. The barrel electromagnetic calorimeters are housed in the barrel cryostat around the inner detector cavity, whereas the barrel and extended barrel hadronic calorimeters are contained in an outer support cylinder. In the end-cap regions, both the electromagnetic and hadronic end-cap calorimeters are housed in the end-cap cryostats together with the integrated forward calorimeters. All calorimeters with the exception of the FCal have pre-shower counters used to distinguish between photons and electrons, and determine whether a shower has been initiated in the wall of the cryostat prior to reaching the calorimeter. Pre-shower counters are also used for calibration purposes. All cryostats are filled with liquid argon and all detectors housed in them are LAr sampling calorimeters. The total absorber thickness of the ATLAS calorimetry system in front of the muon spectrometer is shown in Figure 4.7.

Barrel and extended barrel

The barrel electromagnetic calorimeter uses lead absorber plates, clad between two thin stainless steel sheets, in an 'accordion' geometry (see Figure 4.8) and covers the central pseudo-rapidity range $|\eta| < 1.475$. Fine segmentation in the barrel electromagnetic calorime-

Figure 4.7: *Total absorber thickness of the ATLAS calorimeters. The top curve shows the total thickness in front of the muon spectrometer. Each curve below it gives the contributions of each calorimeter. The discontinuities show transitions between detectors.*

Figure 4.8: *Transverse view of the active part of the barrel EM calorimeter.*

ter is required primarily to distinguish electrons and photons from hadronic jets and therefore the granularity of this detector is: $\Delta\eta \times \Delta\phi = 0.003 \times 0.1$ in the first sampling section, $\Delta\eta \times \Delta\phi = 0.025 \times 0.025$ in the second, and $\Delta\eta \times \Delta\phi = 0.025 \times 0.05$ in the third sampling section.

The barrel and extended barrel hadronic tile calorimeters use plastic scintillator plates embedded in an iron absorber, and cover the ranges $|\eta| < 1.0$ (barrel) and $0.8 < |\eta| < 1.7$ (extended barrel). For a heavy Higgs with a mass of 800 GeV, the reconstruction of jets from the decay of a high-p_{T} W to jet pairs with typical separation $\Delta R = 0.4$ sets the scale for the granularity of the detector.[2] The segmentation of the hadronic tile calorimeters is $\Delta\eta \times \Delta\phi = 0.1 \times 0.1$ in the first and second sampling sections, and $\Delta\eta \times \Delta\phi = 0.2 \times 0.1$ in the third.

End-caps

The end-cap electromagnetic calorimeters, as the barrel electromagnetic calorimeters, use lead absorber plates clad between stainless steel sheets in an 'accordion' geometry. The pseudo-rapidity coverage of the end-cap electromagnetic calorimeter is $1.375 < |\eta| < 3.2$ with fine granularity that is about the same as for the barrel electromagnetic calorimeter up to $|\eta| < 2.5$ and $\Delta\eta \times \Delta\phi = 0.1 \times 0.1$ for $2.5 < |\eta| < 3.2$. The end-cap hadronic calorimeters use copper absorber plates in liquid argon and cover the pseudo-rapidity region

---

[2] The jet separation ΔR is defined as $\Delta R = \sqrt{(\Delta\eta)^2 + (\Delta\phi)^2}$

Figure 4.9: *View of one end-cap calorimeter*

$1.5 \leq |\eta| \leq 3.2$. The segmentation of the end-cap hadronic calorimeter is $\Delta\eta \times \Delta\phi = 0.1 \times 0.1$.

The capability of the ATLAS calorimetry system to measure missing E_{T} relies strongly on the hermeticity of the detector, meaning close to 4π coverage. The integrated forward electromagnetic and hadronic calorimeters covering the region $3.1 \leq |\eta| \leq 4.9$ are essential for this. Since jets in the forward region have high longitudinal momentum and low-p_{T}, coarser segmentation and lower transverse energy resolution is allowed. The granularity in the forward calorimeter is of about $\Delta\eta \times \Delta\phi = 0.2 \times 0.2$. A detailed discussion of the FCal is presented in Chapter 5.

The total energy resolution for photons of $E_{\mathrm{T}} = 50$ GeV at the LHC design luminosity (10^{34} cm^{-2}s^{-1}), including the contributions from the sampling term, the constant term, electronic noise and pile-up, is shown in Figure 4.10. The electronic noise contribution (dotted line), decreases with η. The pile-up contribution (stars), increases with η due to the rise in particle density. The constant term (dashed line), does not vary with η and the sampling term is shown by the circles. The sum of these is the total resolution and it is

Figure 4.10: *Total energy resolution, and contributions from the various terms, as a function of* η *for photons of energy* $E_{\mathrm{T}} = 50$ GeV*.*

shown by the black dots.

Figures 4.11 and 4.12 show features of the hadronic calorimeters in the end-cap region. Figure 4.11 is a plot of the energy resolution for pions in the hadronic end-cap calorimeter prototype as a function of energy. The experimental data points are denoted by black dots and the other symbols denote the results of different Monte Carlo simulations using the `GEANT` framework. The best simulation programs available for simulating hadronic interactions in a detector are G-FLUKA, G-CALOR and G-GHEISHA. As can be seen in Figure 4.11, the results of the simulations do not agree with one another, nor do they agree with the data very well over the relatively small range of about 225 GeV shown in the plot. G-CALOR seems to be in closest agreement with the data, and G-FLUKA seems in furthest agreement over the range from 0 to 225 GeV. These disagreements stem in part from the difficulty in capturing the complexity of the interactions involved in hadronic showers.

Figure 4.12 is a plot of the energy resolution for jets of constant E_{T} of 100 GeV as a function of η. Here, the solid line shows the expected resolution, the white squares show the resolution when using the energy deposited in a cone of $\Delta R = 0.4$ and the black dots

Figure 4.11: *Energy resolution for pions in the hadronic end-cap calorimeter prototype module, compared to the different simulation predictions.*

show the energy resolution using all the energy deposited in the calorimeter. The resolution for a cone of $\Delta R = 0.4$ is considered because it is often necessary to apply cone cuts for identification purposes. This restricts the sensitive elements used for the reconstruction of the event and thus the resolution is not as good as when no cuts are applied.

4.2.4 Trigger and Data Acquisition

An experimental trigger is used to select interesting events for recording and later analysis. The ATLAS trigger and data-acquisition (DAQ) system uses three levels of online triggers. At each trigger level, the decisions made at the previous level are refined, and additional selection criteria can be applied. From the initial bunch crossing rate of 40 MHz corresponding to an interaction rate of 1 GHz, the rate of selected events must be reduced to about 100 Hz for permanent storage. Figure 4.13 shows a simplified view of the trigger and DAQ system. The information in this section is taken from reference [38].

Level 1 selects events by applying certain criteria based on information from a subset of

Figure 4.12: *Energy resolution for jets of* $E_{\mathrm{T}} = 100\,\mathrm{GeV}$ *as a function of* η

detectors from 1 GHz to about 75 kHz. For example, high-p_{T} muons are identified using only certain parts of the muon spectrometer. In the case of the calorimeter selection, reduced-granularity information from all the calorimeters is used. The calorimeter trigger searches for objects like high-p_{T} electrons and photons, jets, and τ-leptons decaying into hadrons, as well as missing and total transverse energies which are calculated by summing over trigger towers (groups of detector elements). The level 1 trigger decision is based on combinations of objects required in coincidence or on veto.

The unique identification of the bunch crossing of interest is an essential requirement of the level 1 trigger. This is not an easy task given that the bunch crossing interval is 25 ns. For the calorimetry system the signal pulse shape extends over many bunch crossings and so information for all detector channels, (more than 10^7 excluding the pixel detectors), is conserved in 'pipeline' memories during the time required for the level 1 trigger to make a decision. The latency (time taken to form and distribute the decision) for the level 1 trigger is $2.0\,\mu$s. [38]

For all events selected by the level 1 trigger, 'region-of-interest' information is provided

Figure 4.13: *Block diagram of Trigger/DAQ system*

to the level 2 trigger to assist in reducing the event rate from 75 kHz to about 1 kHz. Finally level 3 applies the final selection criteria to store event information at a rate of about 100 Hz. This corresponds to an output data rate of about 100 MB/s.

The anticipated data volume of about 1 PByte (10^{15} Bytes) per year will require new methods for data reduction, data selection and data access for physics analysis. It is estimated that for the whole ATLAS software-development project, up to 1000 person-years will be required. [38]

Chapter 5

The ATLAS Forward Calorimeter

In this chapter, a description of the requirements and basics features of the FCal is given in Section 5.1, and a more detailed statement of the components and construction of FCal3, the second hadronic module, is made in Section 5.2. Attention is turned to issues related to the cabling of FCal3 in the latter part of Section 5.2

5.1 The Forward Calorimeter

5.1.1 Basic Requirements

The primary role of the FCal in the ATLAS detector, is to complete the hermeticity of the calorimetry system. Forward calorimetry is important for jet identification and for detecting missing transverse energy ($E_{\mathrm{T}}^{\mathrm{miss}}$). The location of the FCal, about 5 m from the interaction point, permits coverage in the pseudo-rapidity range $3.1 \leq |\eta| \leq 4.9$ in ATLAS, but poses important restrictions on the design of the detector. This section will give an overview of the forward calorimeter and of its physical parameters.

Figure 5.1 shows the detectors inside the end-cap cryostat with electromagnetic and hadronic end-cap wheels and the forward calorimeters along the core of the cryostat. The layout of the FCal positioned within the forward tube structure of the end-cap cryostat is

Figure 5.1: *Layout of detectors inside the end-cap cryostat.*

Figure 5.2: *Cross-sectional view of the FCal housed in the support tube. The EM module in medium gray is on the left, followed by the two hadronic modules in dark gray. The light gray module on the right is a non-instrumented copper 'plug' which provides extra shielding for the muon system. [39]*

shown in Figure 5.2. At this location near the IP and at large rapidity, particle density is very high and the FCal must withstand radiation doses up to 10^6 Gy/yr and a flux of neutrons with kinetic energy $> 100\,\mathrm{keV}$ of up to $10^6\,\mathrm{kHz/cm^2}$. At high energy hadron colliders like the LHC, particle densities and energies are largest at high η, near the forward and backward directions. At every 25 ns beam crossing, 7 TeV of energy is deposited in the FCal which is equivalent to 45 Watts of heat. The only detector technology that can survive in such a harsh environment is calorimetry. [39] Thus the FCal has a simple design and is composed of materials that are all radiation damage resistant.

The FCal has been designed with readout segmentation of order $\Delta\eta \times \Delta\phi = 0.2 \times 0.2$ and with a transverse energy resolution of $\sigma(E_\mathrm{T})/E_\mathrm{T} < 10\%$ for $E_\mathrm{T} > 100\,\mathrm{GeV}$. This E_T resolution requires an overall energy resolution of $\sigma(E)/E < 7\%$ and jet angular resolution of $\sigma(\theta)/\theta < 7\%$. [39]

5.1.2 Dimensions and Physical Parameters

The FCal is a liquid argon, ionising, sampling calorimeter with cylindrical geometry placed directly on the beam axis. It consists of a group of three modules; one electromagnetic, FCal1, and two hadronic, FCal2 and FCal3, and a plug/absorber. All modules have identical outer radii and length along the beam direction. There are two FCal's, placed on either side of the IP, and they are referred to as FCal-A and FCal-C.

A unique feature of the FCal is its electrode design. The basic electrode element used in all modules is a tubular electrode, with axis in the direction of the beam line, consisting of a rod held within a tube and spaced with a PolyEther Ether Ketone or PEEK fibre wound around it. This design allows a very small LAr gap, leading to fast signals and reduced pile-up.

FCal1, the electromagnetic module, has a LAr gap of $250\,\mu$m and the triangular current pulse at the electrode has a full drift time of 50 ns. FCal2 and FCal3, the two hadronic modules, have gaps of $375\,\mu$m and $500\,\mu$m, and drift times of 75 ns and 100 ns respectively.

This is a short drift time compared with 400 ns for the more conventional 2 mm gap in many LAr sampling calorimeters. In the case of FCal1, after just 25 ns, 75% of the signal has already accumulated on the electrode and the readout and electronics shape this pulse to a peaking time of about 40 ns. This electrode design also permits the small precision gaps to be maintained more easily than in conventional parallel plate calorimeters. [39]

Since the FCal1 module is closest to the IP of the three modules, it has the largest number of electrodes and readout channels and the smallest gap. Larger LAr gaps in FCal2 and FCal3 are allowed since the ionisation density from showers decreases with depth. FCal1 is being built at the University of Arizona. Each FCal1 module consist of 19 absorber plates, 12260 electrodes elements, and has a mass of about 2.14 tons.[1] All FCal1 components are made of copper.

FCal2 is placed immediately after FCal1, away from the IP, and FCal3 after it. Both hadronic modules are being built in Canada; FCal2 at the University of Toronto and FCal3 at Carleton University. The hadronic detector modules have total masses of 3.83 and 3.68 tons for FCal2 and FCal3 respectively. They both consist of two copper end plates, one at each end, and an absorber matrix of tungsten slugs filling the volume in between the electrode elements. The electrode elements have tungsten rods and copper tubes. FCal2 has 10200 electrodes and FCal3 has 8224. Figure 5.1 shows the layout of the sub-detectors housed in the end-cap cryostat, and Tables 5.1 and 5.2 give a summary of the dimensions and the physical parameters of the ATLAS forward calorimeter.

---

[1] In fact, FCal1-C has 18 absorber plates and FCal1-A has 19. This is due to slight warping of some of the plates used in the C module. The total depth of material in each module is however the same.

Table 5.1: *FCal physical parameters summary. The depth of each module in radiation lengths and in nuclear interaction length has been re-calculated using the actual masses of the FCal-C modules.*

Parameter	FCal1	FCal2	FCal3	FCal total
$\frac{dE}{dx}$ Sampling Fraction (%)	1.49	1.36	1.68	—
$\frac{dE}{dx}$ Sampling Frequency (cm^{-1})	0.59	0.36	0.34	—
Depth (χ_0)	27	90	88	205
Depth (λ)	2.4	3.3	3.1	8.8
Drift time at the nominal V (ns)	50	75	100	—
Potential across gap (Volts)	250	375	500	—
Electric field across gap (kV/cm)	10	10	10	—
Electrode capacitance (pF)	379	276	227	—

Table 5.2: *FCal dimension summary. The term 'warm' and 'cold' refer to room temperature and LAr temperatures, (about -89*C*) respectively. The location of the module front and rear face is with respect to the IP defined as* $z = 0$.

Dimension	Unit	FCal1	FCal2	FCal3
Module outer radius				
warm	mm	450.75	450.75	450.75
cold	mm	455	455	455
Module inner radius	mm	72	79	86
Module length				
warm	mm	445.5	445.5	445.5
cold	mm	444.2	444.2	444.2
Location of module front face				
warm	mm	4662.5	5119	5595.5
cold	mm	4668.5	5123	5597
Location of module rear face				
warm	mm	5114	5570.5	6047
cold	mm	5120	5573	6047.5
Pseudo-rapidity of front face				
inner edge	η	4.87	4.87	4.87
outer edge	η	3.02	3.12	3.20
Pseudo-rapidity of rear face				
inner edge	η	4.96	4.95	4.95
outer edge	η	3.12	3.20	3.28
Tube to tube spacing	mm	7.5	8.179	9.0
Rod diameter	mm	5.0	5.125	6.0
LAr gap	μm	250	375	500
Number of tubes		12260	10200	8224
Absorber material		Copper	Tungsten	Tungsten
Module mass	ton	2.14	3.83	3.68

5.2 FCal3 Construction

The construction of FCal3-C began in the summer of the 2001 at Carleton University. FCal3-A construction has been underway since late spring of 2002. Section 5.2.1 provides descriptions of the components of FCal3, and since one of a hadronic calorimeter's most essential feature is its total mass, the mass contributions of the components that make up the module are stated. Furthermore, it is important to note that great care and attention has been taken to minimise the number of shorted electrodes in the detector at every stage of the quality control, cleaning, inspecting and assembly. The extensive measures used to ensure a successful module construction, stem from the experience acquired during the construction and testing of the prototype FCal modules. The surface of copper tends to produce particulates and it was found that even the smallest copper flake or metallic dust particle in the gaps between the tubes and rods can cause electrical contact between the two electrode elements. A detailed discussion of issues related to the cabling of the FCal is presented in section 5.2.2. This has been the author's main contribution to the project.

5.2.1 Components

FCal3 is composed of copper end-plates and tubes, tungsten slugs and rods, copper inner and outer absorbers fastened with stainless steel screws, gold plated brass signal, ground and retention pins, PEEK fibres and washers, brass/polyimide printed circuit interconnect boards (ICB's) with gold plated brass contacts and lead-tin solder, miniature Cu coaxial cables coated with polyimide, and polyimide capped stainless steel standoffs.

The paragraphs that follow describe the features, functions and mass contributions of the components of the detector. The discussion focuses on FCal3 and its components but can easily be extended to FCal2, whose structure differs from that of FCal3 only in the dimensions of its internal geometry.

End-plates

There are two precision drilled, 23.5 mm thick absorber Cu end-plates, with 8224 holes each. The FCal3 end-plates weigh about 55 kg each and were machined at the Carleton University Science Technology Centre (STC).[2] The Cu absorber end-plates provide a support structure for the tubes that contain the anode rods, and around which the slugs are laid. A thin groove 300 μm in depth has been machined in each hole, a few millimetres from the edge of the face of the end-plates, in order to add rigidity to the module by swaging the tubes into the end-plates. Tubes in the inner and outer rows were swaged at both ends to provide additional structural strength. The other tubes were swaged at one end only to avoid warping of the end-plates.

The quality control of the end-plates was done by numerous precision measurement, and like all Cu and W module components, the end-plates were cleaned in an ultra-sonic bath with multiple stages using commercial solvent, and reverse osmosis (RO) filtered water for rinsing.

Tubes

Every anode rod is inserted into a Cu tube swaged into the end-plates. There are 8224 copper tubes that have a nominal diameter, length and mass of 7.0 mm, 445.4 mm and 21.8 g respectively. The combined mass of the copper tubes is 179 kg.

The tubes are electrically connected to the end plates by swaging and are thus grounded. A potential difference of 500 V between the tubes and anode rods provides an electric field of 10 kV/cm across the LAr gap.

The procedure involved in preparing the copper tubes for insertion into the module is probably the most time consuming part of the entire module assembly. The copper tubes are first deburred at both ends and inspected visually, then cleaned in the ultra-sonic bath using the commercial solvents LPS and Citranox, and RO water for rinsing. Following this,

---

[2] All Cu plates used in the construction of FCal1, FCal2 and FCal3 were machined at the STC.

Figure 5.3: *FCal3-C end-plates mounted on assembly stand in clean room at Carleton University.*

(a) Sintered tungsten slugs

(b) Two rows of slugs are laid between rows of tubes

(c) Interstacked rows of tubes and slugs

Figure 5.4: *Stacking of FCal3-C in clean room at Carleton University.*

the tubes are swabbed twice and inspected visually once more. Tubes that have any internal or external dust or residue after two swabbings are re-cleaned and re-swabbed. Tubes that appear clean are bagged and moved into the clean room. In the clean room, each tube is inspected twice, the second time by an experienced tube inspector. If any particles are found inside or on the surface of the tube, it is cleaned and swabbed once again. If any defect like dents or scrapes are noticed, the defective tube is rejected and set aside. A roll test is made on each tube to assure straightness within a millimetre or so. One last inspection of the outside surface is done under a magnifying glass prior to insertion to ensure that there are no dents. Once the tube has been inserted and swaged, two final swabs, one from either end of the module, are done to collect any possible copper particles generated by the swaging. A typical tube in the module has been cleaned twice and swabbed five times .

Slugs

The tungsten slugs are produced commercially by sintering a mixture of 96.72% W powder with 2.10% Ni, 1.04% Fe, .02% Cu and .01% Mo. There are about 641200 slugs with a combined mass of 1612 kg in each FCal3 module. The slugs used in FCal3 are a combination of two different sizes: the average mass, length and transverse dimension measurements are 2.52 g, 9.88 mm and 8.64 mm respectively, for 70% of the slugs, and 2.65 g, 9.97 mm and 9.02 mm for the remaining 30%.[3] The tungsten slugs form the absorber matrix and make up about 44% of the total mass of FCal3. Both MiTech Metals and Kulite Tungsten Corporation have produced slugs for the hadronic FCal modules.

The quality control of the slugs includes a visual inspection of each one and precise measurements on 40 slugs out of every 1000. These include a profile gauge test, and length and density measurements. The data for this QC process are recorded on QC sheets, then entered via a workstation and stored electronically. The slugs are then cleaned following a multi-stage ultra-sonic cleaning procedure, dried and bagged.

Rods

Made of almost pure tungsten, the 8824 anode rods used in FCal3 have a nominal diameter, length and mass of 5.5 mm, 443.5 mm and 202.32 g respectively. Their combined mass is 1664 kg, making up about 45% of the mass of FCal3 and therefore, the tungsten slugs and rods constitute about 90% of the mass of the FCal3 module. Approximately 50% of the rods were manufactured in China and the remainder are from Russia.

The QC performed on the rods includes a visual inspection and roll test, and diameter, length and density measurements. This is followed by ultra-sonic cleaning.

Inner and Outer Absorbers

The one inner and twelve outer absorbers are used to enclose the inner parts of the detector module, forming a uniform and smooth envelope around it. They are made of copper and have a combined mass of 116 kg per FCal3 module. All outer absorbers for FCal2 and FCal3 were machined at the STC. The inner absorber fits in the centre of the module around the beam pipe while the outer absorbers enclose the module.

---

[3] Due to a manufacturing error, a large number of slugs were produced with slightly larger mass and dimensions. In order to use these slugs in the modules, a mixture of smaller slugs had to be used in conjunction with the larger ones to ensure that the slugs will fit in the absorber matrix.

All threaded holes in the absorbers were lined with stainless steel insert coils for additional strength. The cleaning was done in the ultra-sonic bath.

(a) Inner absorber (b) Outer absorbers (c) Mounting outer absorbers

Figure 5.5: *FCal3 inner and outer absorbers.*

(a) Anode or Signal pin (b) Ground pins (c) Retention pins

Figure 5.6: *Signal, ground and retention pins used in FCal3.*

Signal, Ground and Retention Pins

Anode or signal pins, with knurl diameter 2.0 mm and full length 16.0 mm, are inserted in the tip of one end of the tungsten rods. Ground pins with knurl diameter 1.6 mm and full length 14.6 mm, and retention pins with knurl diameter 1.6 mm and full length 8.9 mm, are inserted into the end-plates, on opposite faces of the module. (See Figure 5.7) Ground pins inserted into the signal end-plate provide the electrical ground for the ICB's and cables.

Retention pins inserted into the other end-plate help to fasten the PEEK washers meant to prevent the electrodes from sliding out of the tubes.

There is a total of 8224 signal pins and 7168 ground pins on the signal end of the module, and 7168 retention pins on the non-signal end.

(a) Signal end

(b) Non-signal or IP end

Figure 5.7: *Close up view of the assembled FCal3 module from the signal and non-signal end. The ground pins are inserted in the signal end-plate, and the retention pins in the non-signal face. Tubes are stacked and swaged into the end-plates, and rods with PEEK fibres wound around them are inserted into the tubes. The PEEK fibres are attached to the anode pins, and PEEK retaining washers are pressed onto ground and retention pins to hold the fibres and rods in place.*

PEEK fibre and retention washers

Prior to rod insertion into a tube, a PEEK fibre is wound around each rod and then thermoformed to prevent it from unwinding. The PEEK fibre assures electrical isolation between the rod and tube and has a nominal diameter of 500 μm. The uniform winding of the fibre around and along the entire length of the rod assures a uniform LAr gap and thus a constant electric field between the rod and the tube. PEEK retention washers are placed on ground pins and retention pins in order to prevent the tungsten rods from slipping out of the tubes and keep the fibres in place.

(a) ICB's for FCal3 (left) and FCal2

(b) ICB's with soldered cables

Figure 5.8: *Interconnect boards for FCal3 and FCal2. The unassembled boards and contacts are shown in (a), and the fully assembled ICB's with the soldered contacts and miniature coaxial cables are shown in (b). The FCal3 board is the larger one.*

Interconnect Boards

The FCal InterConnect Boards (ICB's) are glue-less printed circuit boards, with 35 μm thick copper, electro-plated with lead-tin solder set on a polyimide substrate with a thickness of 50 μm. The ICB's have holes populated with gold plated brass receptacles that are then soldered on the signal side of the ICB. Finally, a miniature coaxial cable is soldered on the signal side of each ICB, soldering the ground braid to the ground trace first and then the centre conductor to the signal trace. This is meant to act as a strain relief for the fragile centre conductor.

In FCal3, there are 802 chevron or regular shaped ICB's and 110 irregular shaped ones for a total of 912 readout channels. The irregular shaped ICB's are used along the outer and inner perimeter of the module face.

Miniature coaxial cables

The signals are transfered from the electrodes to the electronics via $25\,\Omega$ copper coaxial cables with polyimide dielectric and insulation. The polyimide insulation consists of a very thin glue-less tape wrapped over the cable.

The signal cables are grouped in bundles of 64 referred to as harnesses. Each harness has a one-hundred pin micro-D connector from which 36 pins are used as ground and 64 as signal. A total of 16 harnesses are used for FCal3, and therefore there are on average 7 unused cables per harness.[4] Further details on the assembly, testing and cleaning of the cables will be given in section 5.2.2.

Standoffs

Stainless steel standoffs are screwed onto the module face to maintain the prescribed distance between FCal2 and FCal3. A polyimide cap covers the end of each standoff to maintain electrical isolation of the modules with respect to one another, and to prevent the production of copper particulates from the contact of the standoffs with the end-plates.

5.2.2 Electronics and Cabling

Electronics

From the face of the modules, the cables are directed outward to the outer absorbers where the harnesses are placed in troughs and directed away from the IP toward the back of the end cap cryostat. The cables are then looped up to the summing boards which are located on the back of the Hadronic End-cap Calorimeter (HEC) module. There are five micro-D connectors (four input and one output) and 64 transformers on each summing board. Signals from four ICB's are transmitted through four $25\,\Omega$ striplines to a summing node via

---

[4] A total of 16 harnesses times 64 cables per harness gives 1024 cables. Only 912 cables are required since there are 912 ICB's. This leaves 1024 - 912 = 112 unused cables. Over 16 harnesses, this makes 7 unused cables per harness on average.

a blocking capacitor. The high voltage is transmitted to the signal cables via a 1 or 2 MΩ resistor. A 1:2 step-up auto-transformer is then used to transform the 6.25 Ω impedance as seen coming out of the summing node back to 25 Ω.[5] The transformer output is then transmitted through another 25 Ω stripline to the output connector. From the output connector of a summing board, the signals are transmitted to the vacuum feedthrough through a bundle of cables similar to the ones used to transmit the signals from the module to the summing board, called pigtails. There are 28 summing boards in all: 4 are used for FCal3, 8 for FCal2 and 16 for FCal1. At the vacuum feedthrough, the signals are transmitted to flex cables through thermally sealed connectors and are carried to the outside wall of the cryostat where they are transmitted to the Front End Boards (FEB). Signals get shaped and stored on an analog Switched Capacitor Array (SCA) in the FEB. It is only after a trigger occurs that the signals are digitised and sent out to the readout.

Organisation

The cabling for the FCal is organised in the following manner. Electrodes are grouped to form a tube groups connected by an ICB. Tube groups are grouped together to form readout tiles and readout tiles are grouped to form trigger towers. There are sixteen sectors or 'phi slices' and each is divided in four trigger towers in eta. All modules have four trigger towers per sector, but the number of electrodes per tube group and the number of tiles per trigger tower, are different for each module.

In FCal3, there are 8224 electrodes, 9 electrodes per tube group, 4 tube groups per tile, and 4 tiles per trigger tower. This makes: 4 cables × 4 tiles × 4 trigger towers, or one harness of 64 cables per sector. The cabling of the whole module then, requires 16 harnesses. In FCal2, there are 10200 electrodes, the number of electrodes per tube group is 6, and there are 8 tiles per trigger tower. This makes: 4 cables × 8 tiles × 4 trigger towers, and thus two harnesses are necessary for each sector or 32 harnesses for the entire module.

---

[5] $Z_{\text{out}} = Z_{\text{in}} \cdot n^2$, so $25\,\Omega = 6.25\,\Omega \times 2^2$

FCal1 has 12260 electrodes and only 4 electrodes per tube group. 64 harnesses are therefore required for its cabling.

Cable layout, ICB mapping and nomenclature

Physics considerations like the electromagnetic shower maximum and minimisation of uninstrumented space between the modules as well as the very large number of cables, demand a careful examination of the layout and mounting of the signal cables. In FCal1, the ICB's and cables are connected on the face closest to the IP, to protect them from the intense radiation that occurs at shower maximum near the rear face of the module. This configuration also minimises the non-sensitive space between FCal1 and FCal2, designed to be 7.2 mm between pins and 15.5 mm between end-plates. Both FCal2 and FCal3 signal cables are connected on the rear face of the modules, further away from the IP. The space between FCal2 and FCal3 is 17.2 mm between pins and 31 mm between end-plates, and the space between FCal3 and the copper plug is 53.6 mm between the pins of FCal3 and the face of the plug.

A full size mock-up of FCal3 was used to determine a suitable cable layout on the module face. The mock-up was also used to determine the angle or direction at which the cables should be soldered onto the ICB's. The ICB's were installed on a full quadrant of the mock-up and cables with diameter of 1 mm were soldered to each ICB. The cables were then grouped and laid out in various ways in order to find the most appropriate configuration.

It was determined that only two soldering angles were required: ‘up’ and ‘down’, defined with respect to a right pointing chevron. The diagram in Figure 5.9 shows the definitions of ‘up’ and ‘down’. Furthermore, it was also determined that all four harnesses used to cable one quadrant in FCal3, were to be laid in the trough aligned with the middle of the next quadrant in the clockwise direction. This is to minimise the difference in path length from ICB to trough for the cables in a quadrant. Figure 5.10 on page 61 shows models of the cable layout on the face of the FCal3 and FCal2 modules. Each curved line running on the

Figure 5.9: *Definition of 'up' and 'down' cable solder direction with respect to a regular chevron shaped ICB.*

module face represents a cable harness.

The mapping of an ICB/cable assembly to a particular location on the face of the module, uses a labelling scheme based on the nomenclature defined in the technical drawing of the module. Figure 5.11 on page 62 shows a quarter section of the technical drawing of FCal3-C. The nomenclature identifies each chevron with its location in a tile within a phi slice. The ICB/cable label identifies the location of each ICB/cable on the module face, to which connector pin the cable is attached, and of which harness it is a member. Such a scheme is essential for the proper installation of the ICB's onto the module face and also for the soldering of the cables to the ICB's.

The following labelling scheme has been used. There are two series of digits for each label, one identifies the cable number, and the other identifies the ICB location. Each cable assembly is identified by specifying the module, the harness, the cable, and the solder direction. The ICB location is identified by specifying the sector, the tile and the chevron number. Here is an example of a label:

C3.05.1.39 UP
05.06.3

(a) Cable layout for FCal3

(b) Cable layout for FCal2

Figure 5.10: *Models for cable layout for FCal3 and FCal2.*
The cables are laid out across the adjacent quadrant (FCal3) or octant (FCal2) in order to minimise the difference in path length from ICB to point of exit at the circumference of the module for neighbouring cables.

Figure 5.11: *Quarter section of FCal3-C from the technical drawing, showing sector 0 to 4, labelled PHI 0, PHI 1, PHI 2, etc., trigger towers labelled 1A, 2A, 3A, 4A, and 2A, 2B, 2C, etc., tiles (four per trigger tower) with numerical addresses, and chevrons labelled 1, 2, 3, 4 within each tile. Irregular shaped ICB's are found on the outside and inside perimeter and are labelled 3C1 to 3C36.*

In the upper row of digits ‘C3’ identifies module C of FCal3. ‘05.1’ identifies the harness number, ‘39’ identifies the cable in this harness, and ‘UP’ refers to the solder angle or cable direction. In the lower series of digits ‘05’ refers to the sector on the module face, ‘06’ refers to the tile number in that sector, and ‘3’ refers to the chevron number within that tile. This nomenclature was chosen by the author and the same nomenclature is used by the FCal2 group in Toronto.

This labelling scheme was used to generate tables for every cable harness and a series of verifications and cross-verifications by members of the group were performed to ensure accuracy. A similar procedure was followed to verify and finalise the FCal2 tables. The assembly of ICB’s and the subsequent soldering of the cables for FCal2 and FCal3 were then done commercially. The assembly included populating all ICB’s with electrical receptacles, soldering the receptacles on the signal side of the boards, soldering the cables to the ICB’s, cleaning the cable assemblies and testing them to ensure proper electrical connections and isolation of signal from ground.

ICB/cable inspection, preparation and cleaning

Upon receipt of the assembled harnesses, a careful inspection of the soldering of each ICB/cable assembly is done, followed by a continuity check. This check is used to verify that there is no short between the signal and ground connections and that the labels identify the correct ICB/cable. Each cable is then cleaned and a signal pin, is inserted in each of the seventeen contacts of the ICB. This is done to decrease the insertion force necessary to press on the ICB’s in place on the face of the module during the cabling of the module. Appendix C describes the inspection, preparation and cleaning of the cable harnesses in detail.

Cable installation

Installation of the cables, scheduled to take place in August of 2002, begins with a high voltage test of each electrode. If shorts or trips are found, the electrodes are pulled out and then repaired or replaced. A recorded capacitance measurement of each electrode element follows, after which the ICB/cables are mounted on the module. A continuity check is then performed to assure that all ICB's are in their designated location, followed by another HV test where the voltage is applied to an entire harness from the micro-D connector and the leakage current is monitored. If shorts or trips are detected, each electrode connected by the 64 ICB's must be probed to determine the defective ones.

The application of the cables will be done one quadrant at a time, and in the counter-clockwise direction (refer to Figure 5.10). Quadrant 3 will be cabled first and the harnesses temporarily attached at the top of quadrant 1. Quadrant 4 will be cabled next and its harnesses attached to their exit point in the middle of quadrant 3, following which quadrant 2 will be cabled and its harnesses attached at their exit point on quadrant 4. Finally, to cable quadrant 1, the harnesses from quadrant 3 will be detached from quadrant 1, quadrant 1 will be cabled and its harnesses attached to their point of exit on quadrant 2, and then the harnesses from quadrant 3 set back into the trough aligned with the middle of quadrant 1. This will complete the cabling of the module.

The schedule of events that will follow the cabling of the FCal can be outlined as follows. A cold test where the modules will be placed in LAr and tested for shorts is scheduled for the fall of 2002. The assembly of the FCal in the support tube will take place around the end of November and a beam test will follow. The final stages include the assembly of the FCal in the end-cap cryostat and of the cryostat into ATLAS.

Chapter 6

Signals from Extra Dimension in ATLAS

Will extra spatial dimensions be revealed at the LHC through the ATLAS detector? Monte Carlo studies have been conducted to determine the likelihood of such an incredibly exciting discovery and the results of some of these are presented in this chapter.

Some studies of the sensitivity of the ATLAS detector are model dependent while some claim to be model independent, meaning that they do not depend on a particular model of ED. Such studies usually involve running a simulation several times, each time varying the value of some of the parameters. The models that have received the most attention are those which allow large extra dimensions like ADD. In these models, the floating parameters are the number of ED and the fundamental mass scale. Since the fundamental mass scale is directly related to the size of the extra dimensions, it is straightforward to get one from the other.

Section 6.1 gives an outline of issues related to the detection of missing transverse energy with an example to illustrate them. In Section 6.2, studies on the sensitivity of ATLAS to ED are discussed and their results summarised. [40] The discussion is primarily concerned with graviton production and graviton exchange, and is followed by some comments on studies of Kaluza-Klein gauge boson production.

6.1 Detecting Missing Transverse Energy

Good measurement of the missing transverse energy is needed for two reasons. Firstly, $E_{\mathrm{T}}^{\mathrm{miss}}$ is an important signal for new physics and secondly, reconstruction of a narrow invariant mass distribution for particles involving neutrinos among their decay products requires good $E_{\mathrm{T}}^{\mathrm{miss}}$ resolution. The reliable and precise measurement of an event with missing transverse energy is related to the performance of the calorimeters: good energy resolution, good response linearity and hermetic coverage are required.

The primary reason to include a forward calorimeter system in ATLAS which extends the coverage to $|\eta| < 5$, is to allow the study of interactions giving rise to missing transverse energy signals, and jet tagging or identification. Signals with missing E_{T} are most often caused by undetected neutrinos, but gravitons propagating into dimensions inaccessible to us, would also leave a missing energy signature. Below is an example taken from the results of a simulation presented in references [26] and [38] which illustrates how missing transverse energy signals are used to reconstruct the invariant mass of the A, one of the Higgs type particles predicted by supersymmetry. Analyses of this kind including missing mass determination, would also apply to other new particles that may be produced at the LHC.

Consider the decay of this neutral particle, $A \rightarrow \tau\overline{\tau}$ over a mass range from 100 to 500 GeV. If E_1 and E_2 are the energies and $\vec{u}_1$ and $\vec{u}_2$ are unit vectors in the average directions of the measured τ-decay products (electrons, muons or jets), and if $p_{\mathrm{x}}^{\mathrm{miss}}$, $p_{\mathrm{y}}^{\mathrm{miss}}$ are the projections onto the x and y axes of the measured $p_{\mathrm{T}}^{\mathrm{miss}}$, then the energy of the two neutrino systems from the two τ-decays $E_{\nu 1}$ and $E_{\nu 2}$, can be obtained by solving the two coupled equations:

$$p_{\mathrm{x}}^{\mathrm{miss}} = E_{\nu 1}(\vec{u}_1)_x + E_{\nu 2}(\vec{u}_2)_x \tag{6.1}$$

$$p_{\mathrm{y}}^{\mathrm{miss}} = E_{\nu 1}(\vec{u}_1)_y + E_{\nu 2}(\vec{u}_2)_y \tag{6.2}$$

From this, the invariant mass of A can be reconstructed as:

$$\mathrm{m}_{\tau\tau} = \sqrt{2(E_1 + E_{\nu 1})(E_2 + E_{\nu 2})(1 - \cos\theta)} \tag{6.3}$$

where θ is the angle between $\vec{u}_1$ and $\vec{u}_2$.
Since $\mathrm{m}_{\tau\tau}$ is very sensitive to the measurement of $p_{\mathrm{x}}^{\mathrm{miss}}$ and $p_{\mathrm{y}}^{\mathrm{miss}}$, an excellent resolution is very important for the mass reconstruction.

The resolution of each component of the $E_{\mathrm{T}}^{\mathrm{miss}}$ four-vector, i.e. $\sigma(p_{\mathrm{x}}^{\mathrm{miss}})$ and $\sigma(p_{\mathrm{y}}^{\mathrm{miss}})$, are defined as $\sigma(\Delta p_x)$ and $\sigma(\Delta p_y)$, where Δp_x and Δp_y are given by:

$$\Delta p_x = \Sigma(p_{\mathrm{x}})_{\mathrm{gen}} - \Sigma(p_{\mathrm{x}})_{\mathrm{rec}} \tag{6.4}$$

$$\Delta p_y = \Sigma(p_{\mathrm{y}})_{\mathrm{gen}} - \Sigma(p_{\mathrm{y}})_{\mathrm{rec}} \tag{6.5}$$

The terms $\Sigma(p_{\mathrm{x}})_{\mathrm{gen}}$ and $\Sigma(p_{\mathrm{y}})_{\mathrm{gen}}$ are the sums of the x and y components of the momenta of all the generated particles (neutrinos and muons excluded) without any pseudo-rapidity restrictions, and the terms $\Sigma(p_{\mathrm{x}})_{\mathrm{rec}}$ and $\Sigma(p_{\mathrm{y}})_{\mathrm{rec}}$ are the sums of the x and y momenta reconstructed from the calorimeters. The sum of all transverse energy in the calorimetry system is given by:

$$E_{\mathrm{T}} = \alpha \cdot E_{\mathrm{T}}^{\mathrm{PRE}} + \beta \cdot E_{\mathrm{T}}^{\mathrm{ECAL}} + \gamma \cdot E_{\mathrm{T}}^{\mathrm{HCAL}} \tag{6.6}$$

where ‘PRE’ represents the pre-shower detector, ‘ECAL’ represents the electromagnetic calorimeter, ‘HCAL’ represents the hadronic calorimeter, and α, β, γ are calibration constants.

Section 9.2.1.3 of the ATLAS detector and physics performance design report [38] states that the resolution of each component of the $E_{\mathrm{T}}^{\mathrm{miss}}$ vector, as calculated at the particle level for A→ $\tau\overline{\tau}$ events with mass $m_{\mathrm{A}} = 150\,\mathrm{GeV}$, degrades from 2.3 GeV to 8.3 GeV if the calorimeter coverage is reduced from $|\eta| < 5$ to $|\eta| < 3$. The resolution of each component of the $E_{\mathrm{T}}^{\mathrm{miss}}$ vector, as obtained with a full simulation of A→ $\tau\overline{\tau}$ events with mass $m_{\mathrm{A}} = 150\,\mathrm{GeV}$, was found to be 7 GeV. The main contributions to this resolution come from the barrel (about 5 GeV), the end-cap region (about 4 GeV) and the forward region (about 3 GeV). The contribution from the forward region is the smallest because transverse energy decreases with increasing rapidity. The parametrisation of the resolution as a function of the total transverse energy measured in the calorimeters obtained from the full simulation over $|\eta| < 3$ is:

$$\sigma(p_{\mathrm{xy}}^{\mathrm{miss}}) = 0.46 \times \sqrt{\Sigma E_{\mathrm{T}}} \tag{6.7}$$

where E_{T} is in GeV. If the restriction in η coverage is removed then the resolution is improved and becomes:

$$\sigma(p_{\mathrm{xy}}^{\mathrm{miss}}) = 0.39 \times \sqrt{\Sigma E_{\mathrm{T}}} \tag{6.8}$$

A more intuitive explanation of why it is necessary to have coverage in the forward region, is that since the energy of particles in jets increases with increasing rapidity, even small angles of incidence with respect to the beam axis will give rise to substantial transverse energy. If these highly energetic particles incident at small angles are not detected and their energy accurately measured, this would translate in false missing transverse energy signals, thus degrading the $E_{\mathrm{T}}^{\mathrm{miss}}$ resolution.

The above example shows how missing E_{T} from two tau decays is reconstructed. In the case of graviton production the signature would be simpler and the calculation easier since there would be a single hadronic jet back to back with missing momentum. The total p_{T} from the jet must be equal to the total $p_{\mathrm{T}}^{\mathrm{miss}}$ carried off by the invisible graviton.

6.2 Sensitivity to Extra Dimensions

It was seen in Chapter 2 that extra dimensions could manifest themselves in a variety of ways that include the production and exchange of Kaluza-Klein gravitons, the production of massive gauge bosons and other KK-resonances, as well as the production of mini black holes and other exotic physics phenomena. Gravitons produced from a high energy collision between two partons would probably disappear into ED and leave a signature of a hadronic jet with unbalanced missing transverse energy. The exchange of a virtual graviton between a pair of quarks or gluons and a pair of vector bosons or fermions, would lead to deviations from known cross-sections that would most likely increase with energy. Massive KK excitations of the SM gauge bosons like the Z^* or W^* would decay through the same channels as the Z and W but would have much larger masses.

A number of studies on the sensitivity of the ATLAS detector to signatures of ED have been done and the results of some of these are discussed below.

6.2.1 Graviton Production

For direct graviton production, the best sensitivity is to a decay mode leading to the signature $jet + E_{\mathrm{T}}^{\mathrm{miss}}$ and so only this class of events will be considered in this discussion. The backgrounds to events of this kind are $jet + \mathrm{W}$ or $jet + \mathrm{Z}$. The integrated cross-section for the processes leading to the production of a jet with transverse energy and to an equivalent amount of $E_{\mathrm{T}}^{\mathrm{miss}}$ for various values of the number of ED δ, and quantum gravity mass scale $\mathrm{M_D}$ is shown in Figure 6.1. The cross-section is given as a function of the transverse jet energy cut and the dominant background of $jet + \mathrm{Z} \rightarrow \nu\nu$ is shown in black. In general, as the transverse jet energy cut is increased it becomes easier to distinguish the signals from the background but the cross-section decreases. The blue lines correspond to different mass scales in the case where $\delta = 2$. As might be expected, the case with the lowest mass scale ($\mathrm{M_D} = 4\,\mathrm{TeV}$) has the largest cross-section. The green indicates the case where $\delta = 3$ and

Figure 6.1: *Integrated cross-section for the processes leading to the production of a jet with transverse energy in conjunction with an equal amount of* $E_{\mathrm{T}}^{\mathrm{miss}}$ *at the LHC for various values of* δ *and* $\mathrm{M_D}$*.* δ *is the number of ED and* $\mathrm{M_D}$=$\mathrm{M_{PL(4+n)}}$ *is the quantum gravity scale.*

each green line is labelled with a mass scale value. The yellow shows the case for $\delta = 4$. Looking at the configuration of the different cross-sections for different combinations of δ and $\mathrm{M_D}$ it becomes apparent that it may be very difficult to distinguish the cross-section for $\delta = 2$ and $\mathrm{M_D} = 5\,\mathrm{TeV}$ from the one for $\delta = 4$ and $\mathrm{M_D} = 4\,\mathrm{TeV}$ for example. Determining δ and $\mathrm{M_D}$ separately likely requires the study of a number of different signals.

Figure 6.2 shows the $E_{\mathrm{T}}^{\mathrm{miss}}$ distribution for the background and the signal events. The total background for all $jet+\mathrm{V}$ is shown in black and signals are shown in red with different symbols corresponding to different combinations of δ and $\mathrm{M_D}$ up to $\delta = 4$ and $\mathrm{M_D} = 5\,\mathrm{TeV}$. As the $E_{\mathrm{T}}^{\mathrm{miss}}$ increases, the signal events stand out from the background but also decrease in number.

Figure 6.2: *Distribution of the missing transverse energy in the background and in the signal events after the selection and for an integrated luminosity of* $100\,\mathrm{fb}^{-1}$*. The contribution of the three main backgrounds is shown together with the signals for several values of (*δ*,* $\mathrm{M_D}$*).*

The selection criteria used at high luminosity are the following:

- Jets with $p_\mathrm{T} \geq 100\,\mathrm{GeV}$ within $|\eta| < 3.2$, in conjunction with $E_\mathrm{T}^\mathrm{miss} \geq 100\,\mathrm{GeV}$.
- Rejection of isolated leptons (efficiency of 98%).
- Final selection of events using a cut of $E_\mathrm{T}^\mathrm{miss} > 1\,\mathrm{TeV}$.

The results of the simulation are based on an integrated luminosity of $100\,\mathrm{fb}^{-1}$, equivalent to about 1 year of data taking at high luminosity ($\mathcal{L} = 10^{34}\,\mathrm{cm}^{-2}\mathrm{s}^{-1}$), and are summarised in Tables 6.1 and 6.2.

Table 6.1 shows the number of background events for each type of background. The dominant one is clearly the $jet + \mathrm{Z}$ with the subsequent decay $\mathrm{Z} \rightarrow \nu\nu$. The reason why the

Table 6.1: *Number of background events in Monte Carlo study on the ATLAS sensitivity to graviton production.*

Number of Background Events			
jet+Z ($\nu\nu$)	*jet*+W ($\tau\nu$)	*jet* +W ($\mu\nu$)	*jet*+W ($e\nu$)
523	151	14	12

Table 6.2: *Summary of Monte Carlo study on the ATLAS sensitivity to graviton production for various combinations of the number of ED and mass scale.*

Sensitivity to graviton production			
δ	$\mathrm{M_D}$ (TeV)	Events	$\mathcal{S}_{max} = S/\sqrt{B}$
2	5	1430	54.0
	7	366	13.8
	9	135	5.1
3	5	705	26.7
	7	131	5.0
4	5	391	14.8
	7	53	2.0

contribution to the background from $jet+\mathrm{W}(\tau\nu)$ is much larger than the contribution from the other two W decay channels is that although the branching fraction for $\mathrm{W} \rightarrow l\nu$ is about 10.5% for all leptons, lepton rejection is efficient only for electrons and muons. The tau has a very short lifetime and often decays to a lepton and two neutrinos making it difficult to identify.

In Table 6.2, the first column labelled δ, shows the number of ED. The second column labelled $\mathrm{M_D}$, shows the multi-dimensional Planck mass or the quantum gravity mass scale in TeV. The third column shows the total number of events selected and the last column gives the sensitivity of the ATLAS detector to signals corresponding to the combination of δ and $\mathrm{M_D}$. Looking at the values of the sensitivity in this last column it is clear that most are well above the discovery limit of 5 and only one is below this limit. But, it is experimentally difficult to disentangle δ and $\mathrm{M_D}$. The above results are taken from studies discussed in references [19], [41], [42].

The sensitivity of an experiment to a particle production process is most often estimated statistically by the ratio of the number of events selected to the square root of the number of background events. It is generally accepted that to claim the discovery of a new particle or interaction, the ratio $S/\sqrt{B}$ must be greater or equal to 5. This is usually referred to as the 5-σ effect and means that if, for example, the result of an experiment is reported as $\hat{x} = 5.85 \pm 0.03$, it is meant that if one were to perform a large number of similar experiments with the same number of measurements per experiment, then the true value x would be in the interval [5.70, 6.00] in more than 99.9% of the cases. [43]

It is important to note that in the ADD model and other similar models, $\delta = 2$ with $\mathrm{M_D} \sim 1\,\mathrm{TeV}$ is disfavoured from astrophysical and cosmological considerations. In fact these constraints, the main one being the cooling rate of the supernova SN1987, indicate that for $\delta = 2$, $\mathrm{M_{PL(4+n)}} > 84\,\mathrm{TeV}$. This and other bounds on the number of ED and mass scale are discussed in references [12], [44], [45].

6.2.2 Graviton Exchange

Graviton exchange between a pair of partons and a pair of fermions or vector bosons will cause deviations from the known cross-sections. The Drell-Yang process $h_1 + h_2 \rightarrow l^+ l^- + X$; an interaction between hadrons that produces a pair of leptons and something else, has a well known cross-section. Deviations from it could be an indication of KK-graviton exchange. Furthermore, deviations from the Standard Model di-lepton and di-photon production cross-section, would also be a possible indication of graviton exchange. The calculation of the cross-sections including the contribution from KK graviton exchange are discussed in references [46] and [47].

The Monte Carlo studies on the di-lepton and di-photon cross-sections the results of which are presented in reference [48], used the following event selection criteria:

- Transverse momentum of each lepton or photon $p_{\mathrm{T}}^{\gamma,l} > 50\,\mathrm{GeV}$ and separation $|\eta^{\gamma,l}| < 2.5$

- Invariant mass of lepton or photon pair has upper limit $M_{\gamma\gamma,ll} < 0.9\mathrm{M}_{\mathrm{PL(4+n)}}$ and lower limit $M^{max}_{\gamma\gamma,ll} \geq M_{min}$ set at 800 GeV or optimised to improve signal to noise.

Figure 6.3 shows four plots of the di-lepton invariant mass distribution, and Figure 6.4 shows the maximum reach at the 5σ level (the discovery limit) for di-lepton production with different combinations of the number of extra dimensions n, and the mass scale $\mathrm{M_S}$. The invariant mass distributions and maximal reach for di-photon production are very similar to the ones for di-lepton production, and are thus not shown here.

Among the conclusions drawn by the authors of the study, as is illustrated in Figure 6.4, was that through the process of di-lepton and di-photon production, the ATLAS detector will permit us to probe theories of gravity with extra dimensions up to a mass scale of about 5 to 6.5 TeV for low luminosity and up to 6.5 to 7.9 TeV for high luminosity, depending on the number of extra dimensions. For each value of n considered there is an optimal lower cutoff on the invariant mass, where the reach in the mass scale $\mathrm{M_S}$ is maximal. Comparing Figures b) and d) of 6.3, it was also found that in order to disentangle the dependence of observables on n from the one on $\mathrm{M_S}$, it is important to go beyond the leading term for the summed graviton propagator. [48] In d) the distributions for $\mathrm{M_S} = 4.7$TeV and $n = 2, 3, 4, 5$ are closer together at 4 TeV than the separation between the distributions shown in c) for the full and leading term graviton propagator calculations. Therefore, for the case of $n = 3$, the leading term calculation for the invariant mass distribution could be confused with the case of $n = 4$ or even $n = 5$. Table 6.3 gives a summary of the sensitivity of ATLAS to graviton exchange. The first column gives the number of ED, the second column labelled $\mathrm{M_S^{max}}$ lists the maximum quantum gravity mass scale for the corresponding number of ED to which the ATLAS detector will have sensitivity, the value of which is given in the last column.

Figure 6.3: *Di-lepton invariant mass distributions. Figures a) and b) show plots of the mass distribution for number of ED* $n = 3$ *and mass scale* $\mathrm{M_S} = 4.7\,\mathrm{TeV}$. *In a) the quark-quark and gluon-gluon contributions are shown separately, and the SM background as well as the total signal+background are shown. Figure b) shows the total signal calculated with the full expression for the summed graviton propagator and the one calculated using only the leading term. The total signal for* $n = 3$ *and different values of* $\mathrm{M_S}$ *are shown in c). Figure d) shows the total signal for* $\mathrm{M_S} = 4.7\,\mathrm{TeV}$ *and various values of* n.

Figure 6.4: *Di-lepton production: maximal reach at the* 5σ *level in the mass scale* $\mathrm{M_S}$ *as a function of the lower cut* M_{min}. *The solid lines represent the reach at low luminosity with integrated luminosity of* $10\,\mathrm{fb}^{-1}$, *and the dashed lines are for high luminosity with integrated luminosity of* $100\,\mathrm{fb}^{-1}$. *Each line is labelled by the number of ED,* n.

6.2.3 Kaluza-Klein Gauge Bosons

A variation on models with TeV scale ED, where only gravitons can propagate in the bulk, allows gauge bosons like the γ, W and Z to propagate in all dimensions. This gives rise to Kaluza-Klein towers of gauge boson excitations observable in four dimensions as massive particles. The constraints on the distortion of electroweak parameters from precision measurements at LEP give a lower limit on the lightest resonance of any gauge boson of about 4 TeV.

According to one study based on a model with only one extra dimension, the leptonic decay of excitations of γ and Z bosons provide a striking signature which can be detected at the LHC. Azuelos and Polesello in reference [49] conclude that with an integrated luminosity of $100\mathrm{fb}^{-1}$ a peak in the lepton-lepton invariant mass will be detected if the compactification or quantum gravity mass scale is below 5.8 TeV. A limit of $\mathrm{M_S} < 13.5\,\mathrm{TeV}$ can be obtained

Table 6.3: *Summary of Monte Carlo study on the ATLAS sensitivity to virtual graviton exchange for various combinations of the number of ED δ, and maximum mass scale* $\mathrm{M_S^{max}}$.

Sensitivity to graviton exchange			
δ	$\mathrm{M_S^{max}}$ (TeV)	Events	$\mathcal{S}_{max} = S/\sqrt{B}$
2	7.9	104	14.2
3	7.2	158	16.0
4	6.8	104	14.2
5	6.5	63	12.8

with an integrated luminosity of $300\,\mathrm{fb}^{-1}$ if no peak is observed. If a peak is observed, the study of the angular distribution of the two leptons may allow ATLAS to distinguish the KK excitations from alternative models yielding similar signatures.

Figure 6.5 shows the invariant mass distribution for electron-positron pairs up to 8 TeV. The SM background distribution is shaded and the peaks shown are contributions from leptonic decays of gauge boson excitations at 4, 5 and 6 TeV.

6.2.4 Summary

There are many models of ED with different phenomenological implications and experimental signatures, and only a few have been presented here. Monte Carlo studies performed by members of the ATLAS collaboration show that the sensitivity of the ATLAS detector to signatures of graviton production, graviton exchange, and KK gauge boson resonances will allow us to probe the parameter space (n, $\mathrm{M_S}$), where n is the number of ED and $\mathrm{M_S}$ is the mass scale at which gravity becomes strong compared with the other forces. ATLAS will allow us to confirm or rule out a number of models of ED for a region of the parameter space up to the following limits: (4, 5 TeV) for graviton production, (5, 6.5 TeV) for graviton exchange, and (1, 5.8 TeV) for KK gauge boson production, all for an integrated luminosity of $100\,\mathrm{fb}^{-1}$. Note that the limit of (n, $\mathrm{M_S}$) = (1, 5.8 TeV) for the sensitivity to KK gauge boson production, is derived from a model that is different from ADD-type models and does

Figure 6.5: Invariant mass distribution of e^+e^- pairs. The lowest lying KK excitation of gauge bosons is at 4 TeV. The standard model invariant mass distribution for e^+e^- is shaded.

not have the constraint of $n \geq 2$.

Chapter 7

Conclusion

The experience of spacetime is possibly the most basic aspect of all experiences. All objects, beings, sounds, light and sensations arise within and are permeated by spacetime, and yet its structure remains one of the most mysterious aspects of our world which warrants detailed scientific investigation. The ATLAS experiment is one tool that will allow us to do this.

ATLAS was originally conceived to uncover the mechanism through which different particles acquire different masses and thus would provide an answer to a question that has puzzled physicists for decades. As a general purpose detector ATLAS is also applicable to a search for evidence of a spacetime structure with multiple extra spatial dimensions.

The LHC and the ATLAS detector will give us the opportunity to investigate many aspects of the fundamental interactions between the constituents of matter, and through this, allow us to test and verify the validity of assumptions made in order to explain basic physical phenomena. Testing of models that are based on scientific intuition and speculative assumptions is essential for a more complete understanding of the physical world.

A number of models which include extra spatial dimensions have experimental consequences at the TeV energy scale and will therefore be tested at the LHC with the ATLAS detector. Sensitivity studies have shown that the observation of signals from graviton production, graviton exchange and KK-gauge boson resonances is possible over a substantial range of LHC energies. This permits testing over a wide range of the models' parameter spaces. The sensitivity of ATLAS to signals of ED with signatures of missing E_{T} relies mostly on the calorimetry system, and the resolution of missing E_{T} relies on the hermeticity of the calorimetric coverage. The forward calorimeter is very important in the achievement of close to hermetic coverage.

The parameters in models like the ADD model are the number of ED, n, and the quantum gravity mass scale, $\mathrm{M}_{\mathrm{PL(4+n)}}$. The assumptions used in the ADD model to explain the reason why there seems to be two fundamental energy scales separated by 16 orders of magnitude are that there are at least two compact ED and that the quantum gravity scale is close to the electroweak scale (between 1 and 10 TeV). Monte Carlo studies of signals of ED in ATLAS show that the parameter space of n and $\mathrm{M}_{\mathrm{PL(4+n)}}$ can be probed up to the case of $n = 4$ and $\mathrm{M}_{\mathrm{PL(4+n)}} = 5\,\mathrm{TeV}$ for graviton production, and up to $n = 5$ and $\mathrm{M}_{\mathrm{PL(4+n)}} = 6.5\,\mathrm{TeV}$ for graviton exchange in ADD-type scenarios. The production of KK gauge bosons in an alternative scenario with one ED can be probed up to a mass scale of 5.8 TeV. All the above limits are based on an integrated luminosity of $100\,\mathrm{fb}^{-1}$.

The construction of the ATLAS detector is well under way and on schedule. All FCal-C modules are at CERN and the capacitance testing on the FCal3-C electrodes has been started. The next step will be the cabling of the module. Work on the cabling of FCal2 and FCal1 will follow.

In 2007, the startup of the LHC and of ATLAS will mark a new beginning in the science of high energy physics that will undoubtably revolutionise our current understanding of the universe and of its constituents, and even possibly reveal a hidden spacetime structure with multiple extra dimensions.

Appendix A

Pseudorapidity

The pseudorapidity is an angular variable defined as

$$\eta = -\ln\left[\tan(\theta_{\mathrm{CM}}/2)\right] \tag{A.1}$$

where θ_{CM} is the scattering angle in the centre of mass frame.

The rapidity is defined as

$$y = \frac{1}{2}\ln\left(\frac{E + p_{\mathrm{L}}}{E - p_{\mathrm{L}}}\right) \tag{A.2}$$

where E is the energy and p_{L} is the longitudinal momentum, i.e. momentum along the axis of propagation.

The pseudorapidity η is a useful approximation to the rapidity in cases where the mass and momentum of a particle are not known, and it is used with the azimuthal angle ϕ to represent the direction of an outgoing particle with respect to the interaction point.

Since both y and η are invariant under a Lorentz transformations, they are useful in the parametrization of collisions between hadrons where the center of mass frame is not the same as the lab frame.

Figure A.1 shows the relationship between the pseudo-rapidity and the scattering angle in the center of mass frame. We see that a range of angles from 1 to 90 degrees corresponds approximately to the pseudo-rapidity range 0 to 5 where, a pseudo-rapidity of 0 corresponds to a scattering angle of 90 degrees.

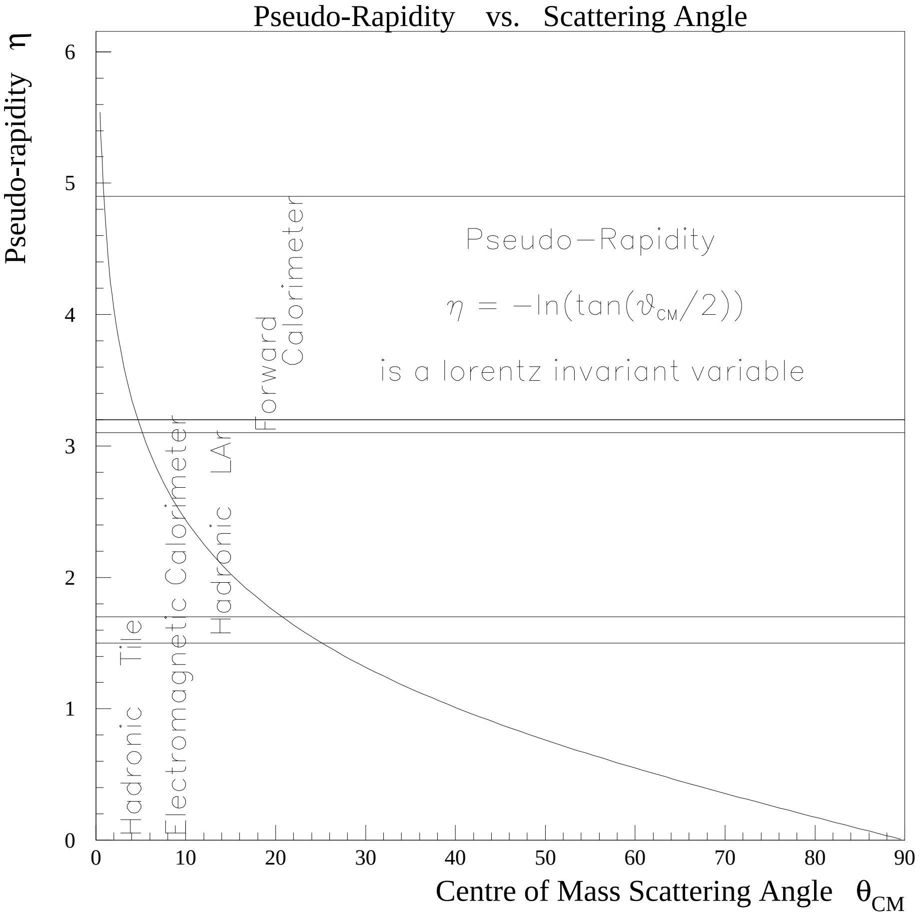

Figure A.1: *Plot of* η *vs.* θ_{CM}*, the pseudorapidity versus the scattering angle in the centre of mass frame. The detector components of ATLAS and their respective range of* η *coverage are indicated on the felt side of the plot.*

Appendix B

The Metric Tensor $g_{\mu\nu}$

A simple and useful way to conceive of a tensor is to view it as a mathematical structure which holds information in the form a an array of numbers. Tensors are usually represented as a letter followed by upper ($T^{\mu\nu}$), lower ($T_{\mu\nu}$), or mixed indeces ($T^{\mu}{}_{\nu}$). The number of indices can be interpreted to correspond to the dimensionality or the rank of the tensor. In this case two indeces describe a two dimensional tensor or second rank tensor. A scalar is a tensor of rank zero, and a vector is a rank one tensor. It is therefore natural to represent a second rank tensor, (a tensor with two indeces), as a matrix. The *metric tensor* is a set of numbers, that contain information about some of the characteristics of the spacetime on which it is defined. The metric tensor is necessary in order to calculate the distance between points.

The dot product combines row and column vectors in a particular way. 'Regular' vectors are represented as column vectors and row vectors are called dual vectors or covectors. The name dual or covector serves to emphasize a correspondance between a given vector and its associated dual vector.

The function of the metric tensor can be viewed as two-fold: If supplied with a vector, the metric tensor will produce the associated dual vector. If supplied with two vectors, the metric will produce a number that will be the scalar product of the two. Simply, the metric tensor provides a mechanism through which two vectors can be combined and their dot product is the result.

To summarize, at the most basic level, the distinction between vectors and dual vectors is not made and two 'vectors' are combined using the dot product to produce a scalar. The reason why the use of a metric is not usually required in everyday calculation is that the metric which describes our everyday three-space is the identity matrix and so a three-vector has the same components as its associated covector. In four-space however the metric tensor is given by the so-called Minkowski metric $\eta_{\mu\nu}$:

$$\eta_{\mu\nu} = \begin{pmatrix} -1 & 0 & 0 & 0 \\ 0 & 1 & 0 & 0 \\ 0 & 0 & 1 & 0 \\ 0 & 0 & 0 & 1 \end{pmatrix} \tag{B.1}$$

and so the associated covector of a four-vector (a_0, a_1, a_2, a_3) is $(-a_0, a_1, a_2, a_3)$, where the time component of the four-vector has changed signs.

Spaces different than our everyday space often have metrics different than the Minkowski metric and so it becomes essential in order to do any calculation involving distances. [1]

---

[1] The word space refers to *a* space, a region of spacetime. "Our" space refers to the space around the earth and one can imagine that since the space around a neutron star or a black hole may be very different than the space around the Earth, the metric tensor used to make calculation in such a space must be quite different than $\eta_{\mu\nu}$.

Appendix C

Cable inspection and cleaning procedures

This process sheet describes the procedure for the cold cable testing and cleaning to be done at Carleton University for all FCAL3 cold cable harnesses.

The most important thing to remember is that great care must be taken in handling the cables. The 64 cables that make up a harness are miniature coaxial cables and have a diameter of less than 1 mm. The center conductor is tiny and very fragile. The outer and inner insulators are made of a thin kapton tape wound around the center conductor (inner), and ground braid (outer). The cables must be handled very delicately and softly. They should not be bent or squeezed tightly.

The procedure begins with the unpacking of the harness from its box and ends with the re-packing of the harness in the same box. Each box is labeled with the harness number found on the connector of the harness. Mindfulness of the order in which the harness boxes are kept is important, in order to keep the process clear and simple. Latex gloves should be worn to handle the cables.

1. Unpacking cable harness.

Open the box, and make sure that there are three QC sheets. They are from Dataplex and should be kept in the box. Pull out the plastic bag that contains the cable harness and carefully take the harness out. Leave the little bag containing small nuts and bolts in the large plastic bag.

2. Connecting cable harness to test unit.

   Carefully unwind the cable harness and lay it flat on the table near the testing station. Carefully take off the small tie and ziplock back covering the connector on the end of the harness and connect it to the test unit. Be very careful in mating the connector ends in order not to damage the pins that are very small and fragile.

3. Connecting test probes.

   If the testing is done by two people it is recommended that one person sits near the test unit and the other near the interconnect boards (ICB's). Each person holds one of the probes from the digital multimeter (DMM). The probe with the alligator clips is used on the test unit and the probe with the pointed tip is used on the ICB's. The person testing the ICB's should have two sheets: one 'Assembly' table for the harness and one QC sheet on which the harness number must be hand written.

4. Preparing ICB's.

   The person handling the cable ends with ICB's should carefully choose a bundle of eight and disentangle it from the other bundles. The ICB's from that bundle should be laid flat on the table and spread out one from the other.

5. Testing ground connections.

   With the alligator probe attached to the ground connection, the metal coaxial connection on the test unit, each ICB ground trace must be tested by touching it with the pointed probe until the DMM emits a audible 'beep'. Each signal trace must also be tested with the pointed probe but no 'beep' should be emitted. Bare cables must also be tested. The ground is the outer metal braid and the signal is the center conductor. If no ‘beep’ is emitted, then make sure that the connections are correct and try it again. Bare cables require a little more attention. If the DMM still does not emit a ‘beep’, make a note of it on the line corresponding to the cable number on the ‘Assembly’ table as well as one the QC sheet.

6. Testing signal connections.

   Following this, each signal connection must be tested individually. Choosing one ICB from the same bundle, read out the cable number written on the small label and verify that it is the same as the last too digits of the top series of numbers on the big label. The metal ‘pin’ on the test unit must be fully inserted in the corresponding test connection. There are 64 test connections, one for each cable. They are grouped in groups of ten, the upper row corresponds to the odd numbers and the lower row to the even numbers. Attaching the alligator clips to the inserted metal pin and touching the signal trace with the pointed probe should cause the DMM to emit a ‘beep’. If it doesn’t, make sure that the connections are correct and try it again. If the DMM still does not emit a ‘beep’, make a note of it on the line corresponding to the cable number on the ‘Assembly’ table as well as on the QC sheet. Test the ground trace to make sure that it does not cause the DMM to emit a ‘beep’. If it does, check the connections and try it again. If it still does take note of it on the corresponding lines on the two sheets. If the connection is good, verify that the series of numbers on the label correspond to the ones on the ‘Assembly’ table and then put a check mark beside the cable number on the table. It is important to verify that the cable has been soldered in the proper direction; UP or DN with respect to a right-pointing ICB. If it is a bare cable, and the big label has a printed series of numbers, then write ‘IRR’ on the corresponding line on the table.

7. Visual inspection.

   When a bundle has been tested, perform a visual inspection of the soldering of the cables and contacts on the ICB's. There should be a uniform solder 'fillet' around each contact and there should not be any pointed tips on the surface of the ICB. There should be no bits of solder or anything inside the contacts. The contacts should be round and undamaged. The center conductor should be soldered in the center of the outside signal trace and the ground braid to the central ground trace. The inner insulator should be centered over the gap between the ground and signal traces.

8. Testing signal connections II.

   Repeat steps 5, 6 and 7 until the entire harness has been tested. When it is finished, staple the two sheets you have been using to the three QC sheets in the harness box. This makes a total of five QC sheets. The topmost sheet should be the QC sheet on which the cable harness number has been written by hand. Any 'bad' connection should be reported to Guillaume or Ernie.

9. Disconnect cable harness.

   Carefully disconnect the cable harness from the test unit using a screwdriver and lifting each side of the connector little by little, alternating sides not to stress the pins. Once disconnected, cover the harness connector with its original ziplock bag and secure it with the tie. Then hang it on the harness hanger in order with respect to the other harnesses on the hanger.

10. Remove tape.

    Tie each bundle of eight cables with a removable plastic tie at the two ends. The tie near the connector end should be tight enough not to slide but not very tight to damage the cables. The tie near the ICB's should be loose enough to slide without restriction along the bundle. Each bundle is taped at many points along the length of the harness. Remove all the tape on the harness.

11. Remove small labels.

    Once all the tape has been removed, using the stainless steel tweezers, very, very carefully remove the small cable number labels stuck to the cables. Do not use force and do not poke or scrape the cable. Moving the tip of the tweezers along the cable, slide it under the label and pull out away from the cable. The labels will unwrap will a little effort. Be very careful not to damage the cable's outer surface.

12. Wipe cables.

    Working with one bundle at a time, untie the plastic tie near the ICB's and using a kimwipe moistened with ethanol, wipe each cable in the bundle from the top to the bottom. Wipe softly in one direction and on all sides of the cable. Wipe many times if necessary but do not wide 'hard'. This will lead to squeezing and possibly kinks in the cable. look closely to make sure that there is no sticky residue left on the cable. Once each cable in the bundle has been wiped clean, tie them with the same tie and repeat the same procedure with each bundle.

13. Final check.

    Once each cable in the harness has been wiped clean, carefully take it off the hanger and place it on the table over the green coloured paper for better contrast. Inspect each cable to make sure that there is no residue left.

14. Re-packing cable harness.

    The cable is now ready to be shipped and must be packed in its box. Carefully roll up the cable in a loose circle taking the time to ensure that the cables do not get entangled. Take a clean plastic bag and insert the harness into it. Fold the top of the bag over and put a piece of plastic tape to keep it closed. Put the bag in the box and close it. The five stapled QC sheets should be placed on top of the bag containing the harness. Place the box with the other 'clean' harness boxes, mindful of the order of the cable harnesses. They should be stacked neatly, away from objetcs that could caused them accidental damage.

Bibliography

[1] Joseph P. et al. Pickett, editor. *The American Heritage Dictionary of the English Language*. Houghton Mifflin Company, Boston, fourth edition, 2000.

[2] Nima Arkani-Hamed, Savas Dimopoulos and Gia Dvali. The Hierarchy Problem and New Dimensions at a Millimeter. hep-ph/9803315, 11 March 1998.

[3] M.E. Pepskin. Theoretical summary lecture for eps hep99. In *International Europhysics Conference on High Energy Physics*, pages 25–33, Tampere, Finland, July 15-21 1999. hep-ph/0002041.

[4] American Linear Collider Working Group. Part 4: Theoretical, Accelerator, and Experimental Options. In *Linear Collider Physics Resource Book for Snowmass 2001*, pages 299–312, 13 June 2001. hep-ex/0106058.

[5] M. Besançon. Experimental Introduction to Extra dimensions. hep-ph/0106165, 20 June 2001.

[6] Y.A. Kubyshin. Models with Extra Dimensions and their Phenomenology. hep-ph/0111027, 2 November 2001.

[7] C. Balázs and B. Laforge. Probing TeV-scale gauge unification by hadron collisions, 16 October 2001.

[8] R.J. Gould. Elementary Theory of Graviton Production Processes. *Annals of Physics*, 238:83–128, 1995.

[9] The OPAL Collaboration. Limits on Low Scale Quantum Gravity in Extra Dimensions from Measuremetns of $e^+e^- \rightarrow e^+e^-$ at LEP2, 23 February 2001. Note PN471.

[10] Donald H. Perkins. *Introduction to High Energy Physics.* Addison-Wesley, 1986.

[11] Nima Arkani-Hamed, Savas Dimopoulos and Gia Dvali. New Dimensions at a Millimeter to a Fermi and Superstrings at a TeV. hep-ph/9804398, 24 April 1998.

[12] Nima Arkani-Hamed, Savas Dimopoulos and Gia Dvali. Phenomenology, Astrophysics and Cosmology of Theories with Sub-Millimiter Dimensions and TeV Scale Quantum Gravity. hep-ph/9807344, 12 July 1998.

[13] E. Mirabelli, M. Perelstein, and M. Peskin. Collider Signatures of New Large Space Dimensions. hep-ph/9811337, 9 February 1999.

[14] T. Rizzo. More and More Indirect Signals for Extra Dimensions at More and More Colliders. hep-ph/9901209, 14 February 1999.

[15] T. Rizzo. Distinguishing Kaluza-Klein Resonances From a Z' in Drell-Yang Processes a the LHC. hep-ph/0109179, 20 September 2001.

[16] The D0 Collaboration. Search for Large Extra Dimensions in Dielectron and Diphoton Production. *Physical Review Letters*, 86(7), 12 February 2001.

[17] C. Allanach, K. Odagiri, M.A. Parker, and B.R. Webber. Searching for narrow graviton resonances with the ATLAS detector at the Large Hadron Collider. *Journal of High Energy Physics*, JHEP 09 (2000) 019, 13 September 2000.

[18] David Griffiths. *Introduction to Elementary Particles*. Addison-Wesley, New York, 1987.

[19] L. Vacavant and I. Hinchliffe. Signals of models with large extra dimensions in ATLAS. *Journal of Physics G: Nuclear and Particle Physics*, 27:1839–1850, 2001.

[20] C. Balazs, D. Dicus, H.-J. He, W. Repko, and C.-P. Yuan. Collider Tests of Compact Space Dimensions Using Weak Gauge Bosons. *Physical Review Letters*, 83(11), 13 September 1999.

[21] S. Dimopoulos and G. Landsberg. Black Holes at the LHC. hep-ph/0106295, 27 June 2001.

[22] T. Banks. A Model for High Energy Scattering in Quantum Gravity. hep-th/9906038, 4 June 1999.

[23] S. Giddings and S. Thomas. High Energy Colliders as Black Hole Factories. hep-ph/0106219, 28 June 2001.

[24] T. Rizzo. Black Hole Production Rates at the LHC: Still Large. hep-ph/0111230, 19 November 2001.

[25] C. Pagliarone. Extra Dimensions and Black Hole Production. hep-ph/0111063, 20 November 2001.

[26] ATLAS Collaboration. ATLAS Calorimeter Performance, December 1996.

[27] Richard Fernow. *Introduction to experimental particle physics*. Cambridge University Press, New York, 1986.

[28] http://rd11.web.cern.ch/RD11/rkb/PH14pp/PH14pp.html.

[29] Peter Loch. *A Brief Introduction into Principles of and Data Analysis for Sampling Calorimeters in High Energy Physics Experiments.* Dept. of Physics, University of Arizona, Tuscon, Arizona 85721, USA, August 25 1998.

[30] The ATLAS Collaboration. ATLAS Letter of Intent for a General-Purpose pp Experiment at the Large Hadron Collider at CERN, October 1992.

[31] The ATLAS Collaboration. ATLAS Technical Proposal for a General-Purpose pp Experiment at the Large Hadron Collider at CERN, December 1994.

[32] The ATLAS LARG unit. ATLAS liquid Argon Calorimeter Technical Design Report (TDR), December 1996.

[33] ATLAS Barrel Toroid Group. ATLAS Barrel Toroid TDR, April 1997.

[34] ATLAS End-cap Toroids Group. ATLAS End-cap Toroids TDR, April 1997.

[35] ATLAS Inner Detector Community. ATLAS Inner Detector TDR, April 1997.

[36] ATLAS Muon Collaboration. ATLAS Muon Spectrometer TDR, May 1997.

[37] ATLAS Tile Calorimeter Collaboration. ATLAS Tile Calorimeter TDR, December 1996.

[38] ATLAS Collaboration. ATLAS Detector and Physics Performance TDR, May 1999.

[39] John Rutherfoord. The ATLAS Forward calorimeters. University of Arizona, Tuscon, Arizona.

[40] G. Bélanger. Model of Extra Dimensions and Their Signals in the ATLAS Detector. In *April Meeting 2002 of the American Physical Society with High Energy Astrophysics Division (HEAD) of the American Astronomical Society*, 2002.

[41] L. Vacavant and I. Hinchliffe. Model Independent Extra-Dimension signatures with ATLAS. hep-ex/0005033, 23 May 2000. ATL-PHYS-2000-016.

[42] G. Azuelos et al. Physics in ATLAS at a possible upgraded LHC, March 8 2001. ATL-COM-PHYS-2000-030.

[43] Glen Cowan. *Statistical Data Analysis.* Clarendon Press, Oxford, 1998.

[44] Thomas Appelquist, Hsin-Chia Cheng, Bogdan A.Dobrescu. Bounds on Universal Extra Dimensions. hep-ph/0012100, 29 June 2000.

[45] S. Hannestad. New Supernova Limit on Large Extra Dimensions: Bounds on Kaluza-Klein Graviton Production. *Physical Review Letters*, Volume 87, Number 5, 11 July 2001.

[46] K. Cheung. Mini-Review on Collider Signatures for Extra Dimensions. hep-ph/0003306, 31 March 2000.

[47] J.L. Hewett. Indirect Collider Signals for Extra Dimensions. *Physical Review Letters*, 82(24), 14 June 1999.

[48] A. Miagkov V. Kabachenko and A. Zenin. Sensitivity of the ATLAS detector to extra dimensions in di-photon and di-lepton production processes. ATL-PHYS-2001-012, 6 September 2001.

[49] G. Azuelos and G. Polesello. Kaluza-Klein Excitations of Gauge Bosons in the ATLAS Detector. In *The Beyond the Standard Model Working Group: Summary Report*, pages 90–108, Les Houches, France, 21 May-1 June 2001. hep-ph/0204031.